REPORT DOCUMENTATION PAGE	Form Approved OM8 No. 0704-0188

1. REPORT DATE (DD-MM-YYYY)	2. REPORT TYPE	3. DATES COVERED (From - To)
04/29/2009	Final Performance Report	01/01/2006 - 04/30/2009

4. TITLE AND SUBTITLE
Spin-Based Devices for Magneto-Optoelectronic Integrated Circuits

5a. CONTRACT NUMBER

5b. GRANT NUMBER
N00014-06-1-0025.

5c. PROGRAM ELEMENT NUMBER

6. AUTHOR(S)
M. Holub, D. Saha, D. Basu, P. Bhattacharya, L. Siddiqui, and S. Datta

5d. PROJECT NUMBER

5e. TASK NUMBER

5f. WORK UNIT NUMBER

7. PERFORMING ORGANIZATION NAME(S) AND ADDRESS(ES)
Professor Pallab Bhattacharya (PI)
Electrical Engineering and Computer Science, University of Michigan, Ann Arbor, Michigan 48109-2122, USA
Professor Supriyo Datta (Co-PI)

8. PERFORMING ORGANIZATION REPORT NUMBER
UM 051977

9. SPONSORING/MONITORING AGENCY NAME(S) AND ADDRESS(ES)
Dr. Chagaan Baatar , Program Officer - Nanoelectronics
Office of Naval Research, Code 312, Room 913,
875 N Randolph, Suite 1425 Arlington VA 22203-1995

10. SPONSOR/MONITOR'S ACRONYM(S)

11. SPONSOR/MONITOR'S REPORT NUMBER(S)

12. DISTRIBUTION/AVAILABILITY STATEMENT
Approved for public release; distribution unlimited

13. SUPPLEMENTARY NOTES
The views, opinions and/or findings contained in this report are those of the author(s) and should not be construed as an official ONR position, policy or decision,unless so designated by other documentation.

14. ABSTRACT
In this project we have designed and demonstrated several fundamental spintronic devices for the first time. The elemental nature of these devices makes them very versatile and they are suitable for wide range of applications. Key results and accomplishments from this research are highlighted below.
• Electrical Injection, Threshold Reduction and Output Circular Polarization Modulation in Quantum Well and Quantum Dot Semiconductor Spin Polarized Lasers working at temperatures up to 200 K.
• Amplification of Spin Current Polarization.
• Electrically Driven Spin-Dynamics of Paramagnetic Impurities: A Spin Capacitor.
• A Monolithically Integrated Magneto-Opto-Electronic Circuit.

15. SUBJECT TERMS
spintronics, spin valve, spin laser

16. SECURITY CLASSIFICATION OF:			17. LIMITATION OF ABSTRACT	18. NUMBER OF PAGES	19a. NAME OF RESPONSIBLE PERSON
a. REPORT	b. ABSTRACT	c. THIS PAGE			P. Bhattacharya, EECS, UM
Unclassified	Unclassified	Unclassified	UL	35	19b. TELEPHONE NUMBER (Include area code) 734 763 6678

INSTRUCTIONS FOR COMPLETING SF 298

1. REPORT DATE. Full publication date, including day, month, if available. Must cite at least the year and be Year 2000 compliant, e.g. 30-06-1998; xx-06-1998; xx-xx-1998.

2. REPORT TYPE. State the type of report, such as final, technical, interim, memorandum, master's thesis, progress, quarterly, research, special, group study, etc.

3. DATES COVERED. Indicate the time during which the work was performed and the report was written, e.g., Jun 1997 - Jun 1998; 1-10 Jun 1996; May - Nov 1998; Nov 1998.

4. TITLE. Enter title and subtitle with volume number and part number, if applicable. On classified documents, enter the title classification in parentheses.

5a. CONTRACT NUMBER. Enter all contract numbers as they appear in the report, e.g. F33615-86-C-5169.

5b. GRANT NUMBER. Enter all grant numbers as they appear in the report, e.g. AFOSR-82-1234.

5c. PROGRAM ELEMENT NUMBER. Enter all program element numbers as they appear in the report, e.g. 61101A.

5d. PROJECT NUMBER. Enter all project numbers as they appear in the report, e.g. 1F665702D1257; ILIR.

5e. TASK NUMBER. Enter all task numbers as they appear in the report, e.g. 05; RF0330201; T4112.

5f. WORK UNIT NUMBER. Enter all work unit numbers as they appear in the report, e.g. 001; AFAPL30480105.

6. AUTHOR(S). Enter name(s) of person(s) responsible for writing the report, performing the research, or credited with the content of the report. The form of entry is the last name, first name, middle initial, and additional qualifiers separated by commas, e.g. Smith, Richard, J, Jr.

7. PERFORMING ORGANIZATION NAME(S) AND ADDRESS(ES). Self-explanatory.

8. PERFORMING ORGANIZATION REPORT NUMBER. Enter all unique alphanumeric report numbers assigned by the performing organization, e.g. BRL-1234; AFWL-TR-85-4017-Vol-21-PT-2.

9. SPONSORING/MONITORING AGENCY NAME(S) AND ADDRESS(ES). Enter the name and address of the organization(s) financially responsible for and monitoring the work.

10. SPONSOR/MONITOR'S ACRONYM(S). Enter, if available, e.g. BRL, ARDEC, NADC.

11. SPONSOR/MONITOR'S REPORT NUMBER(S). Enter report number as assigned by the sponsoring/ monitoring agency, if available, e.g. BRL-TR-829; -215.

12. DISTRIBUTION/AVAILABILITY STATEMENT. Use agency-mandated availability statements to indicate the public availability or distribution limitations of the report. If additional limitations/ restrictions or special markings are indicated, follow agency authorization procedures, e.g. RD/FRD, PROPIN, ITAR, etc. Include copyright information.

13. SUPPLEMENTARY NOTES. Enter information not included elsewhere such as: prepared in cooperation with; translation of; report supersedes; old edition number, etc.

14. ABSTRACT. A brief (approximately 200 words) factual summary of the most significant information.

15. SUBJECT TERMS. Key words or phrases identifying major concepts in the report.

16. SECURITY CLASSIFICATION. Enter security classification in accordance with security classification regulations, e.g. U, C, S, etc. If this form contains classified information, stamp classification level on the top and bottom of this page.

17. LIMITATION OF ABSTRACT. This block must be completed to assign a distribution limitation to the abstract. Enter UU (Unclassified Unlimited) or SAR (Same as Report). An entry in this block is necessary if the abstract is to be limited.

FINAL PERFORMANCE REPORT

Contract/Grant Title : Spin-Based Devices for Magneto-Optoelectronic Integrated Circuits

Contract/Grant # : N00014-06-1-0025.

Reporting Period : 01/01/2006 to 12/31/2008. Ext date : 04/30/2009

Summary of Accomplishments(200 words max):

In this project we have designed and demonstrated several fundamental spintronic devices for the first time. The elemental nature of these devices makes them very versatile and they are suitable for wide range of applications. Key results and accomplishments from this research are highlighted below.

- Electrical Injection, Threshold Reduction and Output Circular Polarization Modulation in Quantum Well and Quantum Dot Semiconductor Spin Polarized Lasers working at temperatures up to 200 K.
- Amplification of Spin Current Polarization.
- Electrically Driven Spin-Dynamics of Paramagnetic Impurities: A Spin Capacitor.
- A Monolithically Integrated Magneto-Opto-Electronic Circuit.

Changes in research objectives, if any: None

Change in ONR program manager, if any : None

Extension granted or milestones slipped if any : Extension granted till 04/30/2009

Include any new discoveries, inventions, or patent disclosures during this reporting period (if none, report none) : None

List of People Involved in, the Publication Stemming from, the Research Effort

- List of participants involved in the research effort
  - PI — Professor Pallab Bhattacharya, Electrical Engineering and Computer Science, University of Michigan, Ann Arbor, Michigan 48109-2122, USA
  - Co-PI — Professor Supriyo Datta, School of Electrical & Computer Engineering, Purdue University, West Lafayette, Indiana 47907, USA
  - GSRAs — Michael Holub, Electrical Engineering and Computer Science, University of Michigan, Ann Arbor, Michigan 48109-2122, USA

    Dipankar Saha, Electrical Engineering and Computer Science, University of Michigan, Ann Arbor, Michigan 48109-2122, USA

    Debashish Basu, Electrical Engineering and Computer Science, University of Michigan, Ann Arbor, Michigan 48109-2122, USA

Lufte Siddiqui, School of Electrical & Computer Engineering,
Purdue University, West Lafayette, Indiana 47907, USA

- Archival publications (published) during the project period:

Journal Papers

1. "Electrical Spin Injection and Threshold Reduction In A Semiconductor Laser", M. Holub, J. Shin, D. Saha, and P. Bhattacharya, *Physical Review Letters,* **98**, pp. 146603.1-4, 2007.

2. "Electrically driven spin-dynamics of paramagnetic impurities", D. Saha, L. Siddiqui, P. Bhattacharya, S. Datta, D. Basu, and M. Holub, *Physical Review Letters,* **100**, 196603, 1-4, 2008.

3. "Optical Polarization Modulation and Gain Anistropy in an Electrically Injected Spin Laser", D. Basu, D. Saha and P. Bhattacharya, *Physical Review Letters.***102**, 093904.1-4,2009.

4. "Epitaxially Grown MnAs/GaAs Lateral Spin-Valves", D. Saha, M. Holub, P. Bhattacharya, and Y. C. Liao, *Applied Physics Letters,* **89**, pp. 142504.1-3, 2006.

5. "Amplification of Spin-Current Polarization", D. Saha, M. Holub, and P. Bhattacharya, *Applied Physics Letters,* **91**(7), pp. 072513.1-3, 2007.

6. "Two Dimensional Spin Diffusion In Multiterminal Lateral Spin-Valves", D. Saha, D. Basu, M. Holub, and P. Bhattacharya, *Applied Physics Letters,* **92**, pp. 022507, 1-3, 2008.

7. "Electrically Injected InAs/GaAs Quantum Dot Spin Laser Operating at 200K", D. Basu, D. Saha, C. C. Wu, M. Holub, Z. Mi, and P. Bhattacharya, *Applied Physics Letters*, **92**, 091119, 1-3, 2008.

8. "A Monolithically Integrated Magneto-Optoelectronic Circuit", D. Saha, D. Basu, and P. Bhattacharya, *Applied Physics Letters,* **93**, 194104, 1-3, 2008.

Conference Papers:

1. "Electron Spin Injection from a Regrown Fe Layer in a Spin-Polarized Vertical-Cavity Surface-Emitting Laser", M. Holub, P. Bhattacharya, J. Shin and D. Saha, *14th International conference on Molecular Beam Epitaxy,* Tokyo, Japan, September 2006.

2. "Magnetoresistance Of Fully Epitaxial MnAs/GaAs Lateral Spin Valves", M. Holub, D. Saha, and P. Bhattacharya, *24th North American Molecular Beam Epitaxy Conference,* Durham, NC, October 2006.

3. "Threshold Current Reduction in a Vertical-Cavity Surface-Emitting Laser via Electron Spin Injection", M. Holub, J. Shin, D. Saha and P. Bhattacharya, *IEEE LEOS Annual Meeting, Montreal,* Canada, October 2006.

4. "Spin Injection and Accumulation In Epitaxially Grown MnAs/GaAs Lateral Spin Valves", D. Saha, M. Holub and P. Bhattacharya, *10th Joint MMM/Intermag Conference,* Baltimore, MD, January 2007.

5. "Measurement of Spin Relaxation Time of Diluted Paramagnetic Mn Impurities in GaAs", D. Saha, M. Holub, and P. Bhattacharya, *North-American Conference on Molecular Beam Epitaxy (NAMBE),* Albuquerque, NM, September, 2007.

6. "Threshold Current Reduction and Output Power Enhancement with Magnetic Field in Sub-Monolayer InAs Quantum Dot VCSELs," D. Basu, D. Saha, M. Holub, Z. Mi, C.C. Wu, and P. Bhattacharya, *IEEE LEOS Annual Meeting,* Lake Buena Vista, FL, October 2007.

7. "Spin-Based Memory Using MnAs/GaAs Multi-Terminal Non-Local Spin Values", D. Saha, M. Holub, P. Bhattacharya and D. Basu, *52nd Magnetism and Magnetic Materials Conference,* Tampa, FL, November 2007.

8. "Threshold Current Reduction and Electrical Modulation of Degree of Circular Polarization in InAs/GaAs Quantum Dot Spin VCSELS," **(INVITED),** D. Basu, C.C. Wu, D. Saha, Z. Mi, and P. Bhattacharya, *Conference on Lasers and Electro-Optics (CLEO),* San Jose, CA, May 2008.

9. "A Spin-Capacitor with Paramagnetic Impurities Embedded in GaAs", D. Saha, D. Basu, and P. Bhattacharya, *Device Research Conference,* Santa Barbara, CA, June 2008.

10. "High-Temperature Spin-Polarized Lasers With Tunnel Spin Injectors," **(INVITED)** P. Bhattacharya, D. Basu, M. Holub and D. Saha, *36th Conference on the Physics and Chemistry of Semiconductor Interfaces (PCSI),* Santa Barbara, CA, January 2009.

11. "Electrically Injected Spin Polarized Lasers," **(INVITED)**, P. Bhattacharya, D. Basu, and D. Saha, *March Meeting of the American Physical Society,* Pittsburgh, PA, March 2009.

1. Quantum Well and Quantum Dot Spin Polarized Lasers

Comprehensive Summary of the significant work accomplished

Spin-polarized lasers are expected to outperform semi-conductor lasers whose operation depends solely on electron charge. Spin-dependent effects such as ultrafast optical switching [1], polarization control [2], and thresh-old current reduction [3] have already been demonstrated in vertical-cavity surface-emitting lasers (VCSELs) using circularly polarized photoexcitation to generate spin-polarized carriers. The ability to independently modulate the optical polarization and intensity in spin-polarized VCSELs (spin-VCSELs) make these lasers suitable for a wide range of applications, including reconfigurable optical interconnects, ultrafast optical switches, chiroptical spectroscopy, and telecommunications with enhanced bandwidth.

Spin-VCSEL operation stems from optical selection rules which govern the conversion between spin and photon angular momentum [4]. [Recombination of spin-up (spin-down) electrons and heavy holes radiates left-hand (right-hand) circularly polarized photons.] The fundamen-tal mode of a VCSEL may be described by two, circularly polarized lasing transitions in which intermixing occurs through spin-flip processes [5], and spin-polarized carriers will couple selectively to one circularly polarized mode to satisfy angular momentum conservation. A randomly polarized current will feed both modes equally such that both modes must reach threshold for lasing to occur. Consequently, both modes radiate equal intensities which admix above threshold to form linearly polarized emission. A spin-polarized current, however, will feed one mode preferentially such that the favored mode can reach threshold with fewer total carriers. Lasing of the unfavored mode is effectively suppressed until the injection current is increased sufficiently to satisfy lasing requirements for both circularly polarized modes. The onset of lasing occurs with fewer total carriers as required for a randomly polarized current, and the overall threshold current of the laser is effectively reduced. Injection of a 100% spin-polarized current is expected to result in a theoretically maximal reduction of 50%. Threshold current reductions have been demonstrated experimentally in optically pumped spin-VCSELs at both low and room temperature [3,6]. However, electrically pumped spin lasers are essential for practical applications. Confirmation of electrical spin injection in VCSELs is nontrivial and complicated by a need to apply large magnetic fields to perpendicularly magnetize most thin-film ferromagnets [7]. In this Letter, we report the first unambiguous demonstration of an electrically pumped spin-VCSEL where an Fe Schottky tunnel contact is utilized for electron spin injection into an InGaAs quantum well (QW) VCSEL. A net degree of circular polarization of 23% along with a significant threshold current reduction of 11% are observed. Rate equation analysis of the observed reduction provides a reasonable estimate of the cavity spin polarization.

Most significant advancements and Conclusions (include equations & figures as appropriate)

The laser sample is grown by molecular-beam epitaxy (MBE) and consists of a 29.5-pair $Al_{0.8}Ga_{0.2}As/GaAs$ distributed Bragg reflector (DBR) stack for the bottom mirror, a full-wave GaAs cavity with an $In_{0.2}Ga_{0.8}As$ multiple QW (MQW) active region, and a hybrid top mirror formed from one quarter-wave pair of p-doped ($N_A = 5x10^{18}cm^{-3}$) $Al_{0.8}Ga_{0.2}As/GaAs$ DBR and a 5-pair $MgF_2/ZnSe$ dielectric DBR stack [7]. For the bottom DBR mirror, only the three $Al_{0.8}Ga_{0.2}As/GaAs$ pairs nearest to the cavity are n-doped ($N_D= 7\ x10^{17}\ cm^{-3}$). Circular

post spin-VCSELs are fabricated using standard microfabrication techniques. We elect annular intracavity contacts for electrical device connection which are interconnected to coplanar anode and cathode bond pads. Such a configuration is commonly used in high-performance VCSELs. An Fe/$Al_{0.1}Ga_{0.9}As$ Schottky barrier is deposited by MBE regrowth around the laser mesas on the topmost n-GaAs layer, which is needed to reduce the transport length from the Fe contact to the active region. We adopt a recipe reported by Hanbicki et al. [8], which results in spin-injection effciencies of 30% over the temperature range of 90–240 K. Control VCSELs where Fe is deposited atop nonmagnetic n-Ohmic metallization and nonmagnetic VCSELs containing no Fe are also fabricated to provide evidence of electrical spin injection in our Fe spin-VCSEL.

The polarization of VCSEL emission is determined by spin and cavity anisotropies, which can either compete or cooperate to determine the laser polarization state [9]. Though cylindrically-symmetric VCSELs ideally lack a polarization anisotropy mechanism to select a preferred polarization, linearly polarized emission aligned along a <110> axis is generally observed and attributed to strain-induced birefringence [10]. This polarization preference is relatively weak, leading to polarization switching induced by changes in temperature, injection current, or stress. Measurements on our VCSELs find a highly linearly polarized emission above threshold with the polarization axis aligned along a <110> direction. In this experiment, we confirm that the spin anisotropy induced from spin injection can overcome unintentional polarization preferences present in our design.

The degree of circular polarization, Π_C, of the Fe spin-VCSEL is analyzed using a photoelastic modulator and linear polarizer combined with lock-in detection. The laser is biased near threshold [$1.2 \times I_{th,0}$ where $I_{th,0}$ is the threshold current at zero magnetic field (H=0)] under continuous-wave (cw) operation and characterized using the Faraday geometry. As shown in Fig. 1(a), Π_C for a 15 μm diameter Fe spin-VCSEL is seen to very closely track the out-of-plane magnetization of a 10 nm Fe layer, which demonstrates that the electroluminescence polariza-tion originates from the Fe contact. Π_C saturates at nearly 23% for applied magnetic fields greater than the out-of-plane saturation field for Fe ($H_{sat} \approx 2.2$T), and the sign of Π_C is indicative of majority spin injection. Since spin injection results in a net circular polarization,

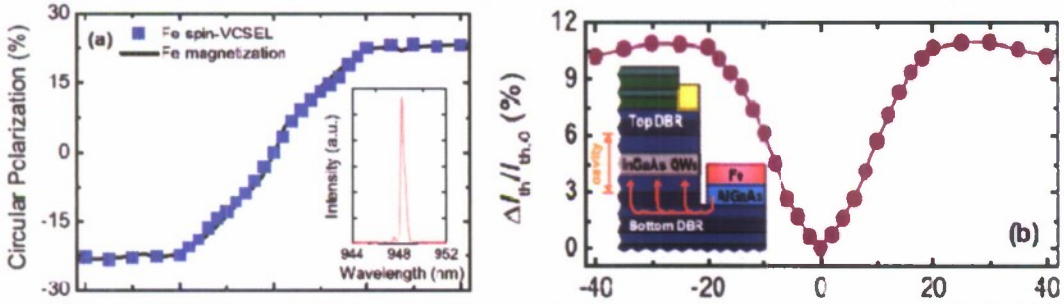

Figure 1 (a) Degree of circular polarization and (b) threshold current reduction versus magnetic field for a 15 μm diameter spin-polarized VCSEL measured at 50 K. The normalized out-of-plane magnetization curve for a 10 nm Fe layer is shown for comparison. Top inset shows the electro-luminescence spectrum, exhibiting a full-width at half maximum of 0.36 nm at 50 K. Bottom inset depicts the Fe spin-polarized VCSEL design.

we conclude that spin anisotropy is sufficient to overcome other anisotropy mechanisms introduced from cavity anisotropy, geometry, or wave guiding effects that impart a preference for linear polarization in the Fe spin-VCSEL.

Longitudinal and transverse optical confinements are ensured by the DBR mirrors and post geometry, respectively, such that the emission never passes through the ferromagnetic Fe

layer. Therefore, a parasitic polarization arising from magnetic circular dichroism (MCD) is absent in our laser since the Fe layer is incorporated outside of the cylindrical resonator; this assumption is verified through magneto-photoluminescence measurements [11]. More-over, a $\Pi_C < 1.5\%$ is measured for magnetic fields up to 40 kOe in the control VCSEL, which is significantly less than the saturation value of Π_C measured for the Fe spin-VCSEL. Parasitic contributions from stray field or magneto-optical effects cannot account for the observed Π_C in the Fe spin-VCSEL, which provides convincing evidence of spin injection, transport, and detection in our Fe spin-VCSEL.

Semiconductor lasers are expected to exhibit a threshold current reduction when pumped with a spin-polarized current. Any change in threshold current (ΔI_{th}) will be reflected by a change in total light intensity (ΔL) for a fixed current bias, and the threshold current reduction may be determined from $\Delta I_{th} = \Delta L/\eta_D$, where η_D is the differential slope efficiency. Magnetic field dependent optical power measurements are performed in the Faraday geome-try for cw-biased Fe spin-VCSELs. As H is increased from 0 to 40 kOe, an emission intensity enhancement and cor-responding threshold current reduction are observed for a 15 μm diameter spin-VCSEL biased at 1.2 $I_{th,0}$ [Fig. 1(b)]. The threshold current reduction saturates for $H > H_{sat}$ at a value of 11%. The gradual decrease of $\Delta I_{th}/I_{th,0}$ at high magnetic fields is attributed to the slight decrease in total light intensity with increasing magnetic field, which is observed for both spin-polarized and non-magnetic VCSELs. The mechanism responsible for this behavior is currently unknown. Negligible threshold cur-rent reductions are observed for the control and nonmag-netic VCSELs [11]. This finding proves that the threshold current reduction results exclusively from electron spin injection by the Fe/AlGaAs Schottky tunnel barrier. As shown in the inset to Fig. 1(b), placement of the spin injector around the laser mesa requires both transverse and longitudinal spin transport for electron spins to reach the laser active region. The separation between the Fe contact and laser mesa is ~1 μm. This results in an average electron spin transport length of ~4.5 μm in a 15 μm spin-VCSEL. The observation of a sizable threshold reduction is in accord with spin transport lengths exceeding 30 μm observed by other groups [12,13].

To analyze the carrier-photon dynamics in our Fe spin-VCSEL, we employ a rate equation model [3,6,14] which accounts for the spin-up and spin-down carrier densities in the barrier, nb , and MQW active region, n, and the photon density for right-and left-circularly polarized light, S.. The rate equations are as follows:

$$\frac{\partial n_b^{\pm}}{\partial t} = -\frac{n_b^{\pm}}{\tau_{cap}} + \frac{1 \pm P_{spin}}{2}\frac{I_{pump}}{qV_b} \mp \frac{n_b^{+} - n_b^{-}}{\tau_{s,b}} \tag{1}$$

$$\frac{\partial n^{\pm}}{\partial t} = \frac{V_b}{V_{MQW}}\frac{n_b^{\pm}}{\tau_{cap}} - v_g g(n^{\pm}, S^{\mp})S^{\mp} \mp \frac{n^{+} - n^{-}}{\tau_s} - B_{sp}\frac{n^{\pm}(n^{+} + n^{-})}{2} - C\frac{n^{\pm}(n^{+} + n^{-})^2}{2} \tag{2}$$

$$\frac{\partial S^{\pm}}{\partial t} = \Gamma v_g g(n^{\mp}, S^{\pm})S^{\pm} + \Gamma\beta B_{sp}\frac{n^{\pm}(n^{+} + n^{-})}{2} - \frac{S^{\pm}}{\tau_{ph}} \tag{3}$$

where τ_{cap} is the carrier capture time, P_{spin} is the degree of spin polarization of the pump current (I_{pump}), $\tau_{s,b}$ is the spin-flip time in the barrier (QW), V_b (V_{MQW}) is the volume of the barrier (active region), B_{sp} (C) is the bimolecular radiative (Auger) recombination coefficient, v_g is the group velocity of light, Γ is the optical confinement factor, β is the spontaneous emission factor, and τ_{ph} is the photon cavity lifetime. The gain in the laser cavity is modeled as $g(n,S)=dg/dn\ (n-n_{tr})/(1-\varepsilon S)$, where dg/dn is the differential gain, n_{tr} is the transparency carrier density, and ε is the gain compression factor. The parameters used in our analysis are estimated from reports on similar structures characterized at cryogenic temperatures and are as follows [15–22]: τ_{cap}=45

ps, $\tau_{s,b}$= 500 ps, τ_s =300 ps, dg/dn =1.1 × 10^{-14} cm/s, n_{tr} = (3.6-4.9)×10^{17} cm^{-3} , ε = 4.5×10^{-17} cm^{-3}, cm, B_{sp} = 9.4 ×10^{-10} cm^3/s, C = 3.8×10^{-29} cm^6/s, v_g = 0.87 × 10^{10} cm/s, Γ=0.029, β = 6 ×10^{-4}, and τ_{ph} =1.25 ps.

A P_{spin} of -19:8% corresponds to a threshold current reduction of 11% for the 15 μm diameter Fe spin-VCSEL discussed above. Figures 2(a) and 2(b) show the light versus current (L-I) characteristics for P_{spin} 0% and -19:8%, respectively, where the total light intensity is the sum of the right-hand and left-hand circularly polarized lasing mode intensities. The threshold currents for the circularly polarized modes $I_{th}^{\pm}$) separate as P_{spin} increases,and the overall laser threshold current is determined by the

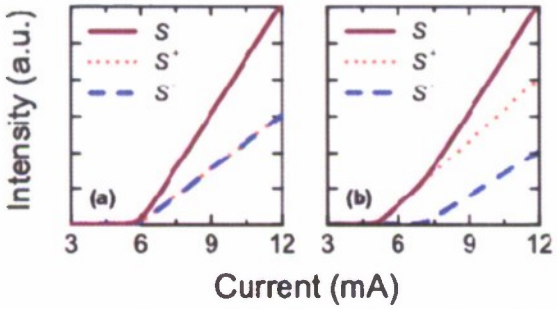

Figure. 2 Theoretical light versus current characteristics for a 15 μm spin-polarized VCSEL driven with (a) 0% and (b) -19.8% spin-polarized pump currents. The solid line represents the total light intensity, S, which is the summation of the right-hand (S^+, dotted line) and left-hand circularly polarized (S^-, dashed line) modes.

favored mode. It can be seen in Fig. 2(b) that a kink in the L-I characteristics is introduced at an injection current value equal to the threshold current of the unfavored mode.

The electron spin polarization in the GaAs barrier ($\Pi_{s,b}$) and InGaAs MQW active region (Π_S) corresponding to P_{spin} -19:8% and evaluated at threshold are approximately -16.8% and -7%, respectively. The barrier spin polarization is found to be essentially independent of bias, determined primarily by P_{spin}, $\tau_{s,b}$, and τ_{cap}. In stark contrast, the quantum well spin polarization is influenced by the value of $g(n^{\pm};S^{\pm})$ and therefore depends strongly on bias. As the pump current increases, .S is seen from the rate equations to decrease rapidly from -7%at $I_{pump} = I_{th}^{+}$ to 0% at $I_{pump} \geq I_{th}^{-}$ This phenomenon occurs since the carrier density for either mode above threshold is essentially fixed at the threshold carrier density. Any additional carriers recombine instantaneously—within the stimulated recombination lifetime —producing stimulated photons. For a pump current $I_{pump} > I_{th}^{-} > I_{th}^{+}$, both circularly polarized modes are lasing and Π_S is negligibly small. The Fe spin-VCSEL circular polarization will instead be determined by $\Pi_{S,b}$ (-16.8% for $H>H_{sat}$).

According to optical selection rules, the degree of electron spin polarization in the active region corresponds to half the degree of circular polarization in bulk material and matches that in quantum wells. While these simple linear relationships hold for spin-polarized light-emitting diodes (spin-LEDs), they are invalid for spin VCSELs when biased above threshold due to optical amplification. A narrow injection current window exists in which the spin-induced gain anisotropy results in large degrees of circular polarization, even for small spin polarizations, through stimulated emission amplification. This effect is demonstrated in our Fe spin-VCSEL for which we measured a Π_C (23%) larger than the cavity spin polarization estimated from the observed threshold reduction (16.8%).

Because of the spin-induced gain anisotropy and result-ing threshold reduction, a spin-VCSEL is expected to exhibit an increase in optical power for a given bias current under spin-

polarized pumping. Here we define the emission intensity enhancement as $\bar{S}= (S+S_0)/S_0$, where S_0 is the total light intensity at H = 0. Figure 3 shows the bias and temperature dependence of S for a separate 15 μm diameter Fe spin-VCSEL under 4.5 kOe. The transparency carrier density is set to 4.9×10^{17} , 4.4×10^{17}, and 3.6×10^{17} cm^{-3} in order to match the threshold current measured at 50, 75, and 100 K, respectively. We calculate $\bar{S}$ at these temperatures where P_{spin} is used as the only fitting parameter. Excellent agreement between the experimental and theoretical values of $\bar{S}$ is found at 50, 75, and 100 K for pump current (cavity) spin polarizations of 5.3% (4.5%), 5.0% (4.2%), and 5.0% (4.2%), respectively. It is evident that $\bar{S}$ peaks at $I_{th,0}$ where switching from an unpolarized to a spin-polarized current can effectively switch the laser between stimulated and spontaneous emission regimes—a form of spin-controlled laser modulation. A discrepancy

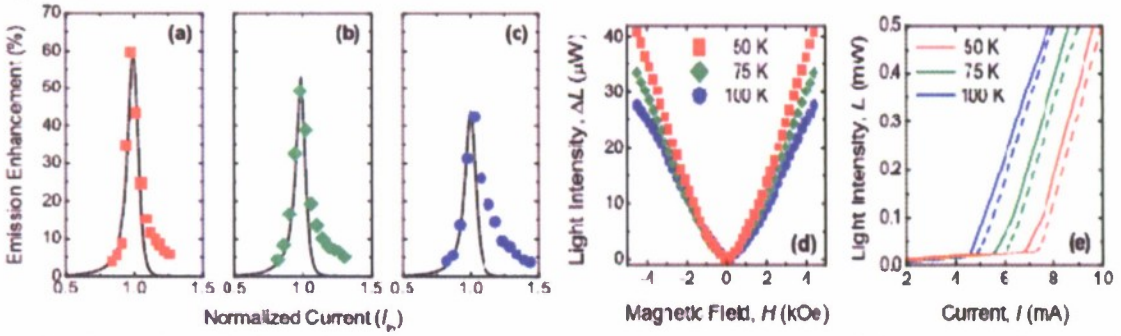

Figure. 3 (color online). Emission intensity enhancement versus normalized current ($I=I_{th}$) measured at (a) 50, (b) 75, and (c) 100K for a 15 μm diameter Fe spin-polarized VCSEL under 4.5 kOe. The solid lines represent the emission intensity enhancement predicted from the rate equation analysis. (d) Light intensity change versus magnetic field and (e) light intensity versus current measured at 0 (dashed line) and 5 kOe (solid line).

between theory and experiment for $\bar{S}$ may be seen at high bias in Figs. 3(a)–3(c). The rate equations predict that the emission intensity for pump currents $I_{pump} \geq \max\{I_{th}^{+};I_{th}^{-}\}$ is the same regardless of the exact value for P_{spin}. We believe this to be a limitation of the model as higher emission intensities are experimentally observed well-above threshold under spin injection. Figures 3(d) and 3(e) show the change in total light intensity (ΔL) and the L-I characteristics, respectively, as a function of magnetic field. The large ΔL (tens of μW) resulting from the increase in slope efficiency with decreasing temperature enables measurement of small threshold current changes. The threshold current reductions at 4.5 kOe as inferred from Figs. 3(d) and 3(e) are 3.8%, 3.8%, and 3.6% at 50, 75, and 100 K, respectively. These values are in reasonable agreement with the reductions suggested from the L-I characteristics and from the rate equation model. The theoretically predicted kink in the L-I characteristics is observed experimentally [Fig. 3(e)] and is attributed to a separation of the circularly polarized lasing modes induced by electron spin injection. We note that higher threshold current densities are mea-sured for our 15 μm VCSELs than for larger mesa diameters, which is commonly observed in etched-posted VCSELs. Scattering and diffractive losses as well as surface recombination become dominant in small diameter etched-post VCSELs, causing the threshold gain to increase [23]. Threshold reductions reported here are mea-sured for individual devices, so the precise value of the threshold current density is unimportant.

Optical Polarization and Gain Anisotropy in an Electrically Injected Quantum Dot Spin Laser Operating at 200 K

The selection rules for the conservation of angular momentum directly relate the spin orientation of the carriers transported to the active region to the polarization of photons emitted upon their radiative recombination [4]. While these relations hold for spontaneous emission, such as in a spin light-emitting diode (LED), they do not reflect the output polarization in a spin laser [6] due to the non-linear dynamics and the spin polarization in the gain medium (active region), which gives rise to a large gain anisotropy at biases near threshold. As a result, the output polarization can be much larger than the spin polarization of the injected carriers. This is intuitively understood and has also been observed by us in quantum well spin lasers [24], but the exact magnitude of the output polarization and the parameters and dynamics upon which it depends have been hitherto unknown. In the present project we have derived the analytical form of the output polarization Π_C , threshold current $I_{th}(H)$, and the threshold current reduction ΔI_{th} $/I_{th,0}$, as determined by gain anisotropy. In particular, we have highlighted the role of the diffusive transport of spin-polarized electrons from the ferromagnetic contact to the active region. The calculated values of these parameters are in excellent agreement with values obtained from the first measurement of electrical modulation of a InAs/GaAs QD spin-VCSEL with MnAs ferromagnetic contacts, schematically shown in Fig. 1. The QD active region allows high temperature operation since the spin relaxation time in the dots, limited by the DP spin

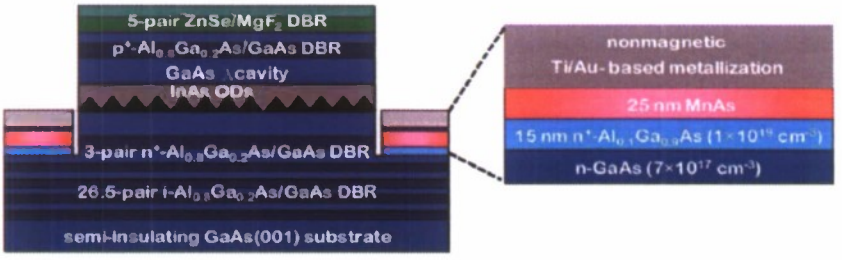

Figure 1: Heterostructure of GaAs-based spin-VCSEL grown by molecular beam epitaxy. The active (gain) region consists of 10 periods of self-organized InAs/GaAs quantum dotsplaced in a GaAs - λcavity. The top DBR mirror consists of 5 pairs of $ZnSe/MgF_2$ deposited by PVD. The ferromagnetic $MnAs/Al_{0.1}Ga_{0.9}As$ tunnel injector contact is regrown selectively on GaAs after a mesa-etch stop, as shown in the figure.

scattering process [25], is enhanced due to carrier confinement. The present study provides a comprehensive insight to the operation and characteristics of an electrically injected spin-polarized semiconductor laser.

An important aspect which has to be taken into account in any spin laser, edge-or surface-emitting, is the diffusive spin transport from the ferromagnetic contact to the active region. Spin polarization at a distance x from the ferromagnetic contact at x = 0 (see Fig. 2) is governed by [26],

$$\frac{\partial^2\left(N^+ - N^-\right)}{\partial x^2} = \frac{N^+ - N^-}{\lambda_{sf}^2} \tag{1}$$

where λ_{sf} is the spin diffusion length in the transport medium and $N^+(x)$ and $N^-(x)$ are the spin-up and spin-down carrier densities at any point x. Drift of spin-polarized carriers is neglected since the doping densities in the transport region is relatively high (5×10^{17} cm^{-3}) [12].

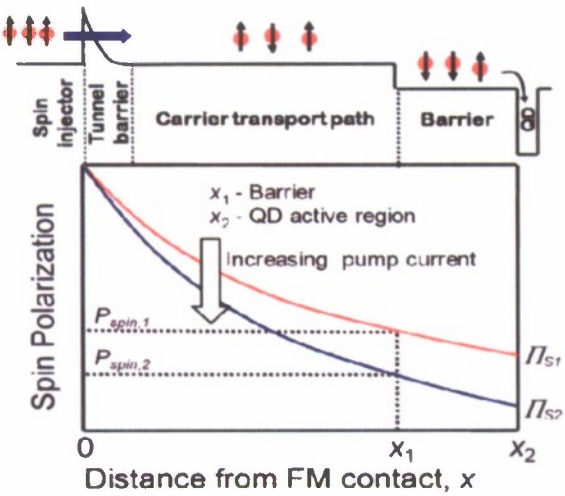

Figure 2: Schematic representation of the variation of carriers spin polarization with distance from ferromagnetic contact (MnAs) in VCSEL in accordance with the spin diffusion equation. The barrier (cavity) is at distance x_1 and the quantum dot region is at distance x_2. The spin polarization decreases with increasing pump current. In the barrier and quantum dots the polarization decreases from $P_{spin,1}$ to $P_{spin,2}$ and Π_{S1} to Π_{S2}, respectively.

These functions are valid from the contact up to the barrier (cavity) region i.e. $x = x_1$. For $x>x1$ the polarization is governed by the laser parameters. Also, we know that the ferromagnetic contact polarization is given by,

$$P_{contact} = \Pi(x=0) = \frac{N^+(x=0) - N^-(x=0)}{N^+(x=0) + N^-(x=0)}$$

The value of $P_{contact}$ is known from a measurement of the out-of-plane magnetization of the MnAs contact as a function of H [27], the spin dependent density of states of MnAs [28] and the spin injection efficiency at the MnAs/GaAs tunnel barrier [29].

The dynamics of carrier and photon densities in semiconductor lasers are governed by the coupled rate equations as outlined in Ref. [6, 30]. The parameters used in the model along with the values for our laser are listed in Table 1. The non-linear gain in the active region is generally expressed in terms of the gain compression factor ϵ as $g(n,S) = dg/dn\ (n-n_{tr})/(1+\epsilon S)$, where n $(=n^+ + n^-)$ is the total (sum of spin-up and spin-down electrons) carrier density in the active region. Since the laser is operated very close to threshold where the gain anisotropy is a maximum, $\epsilon S << 1$, hence $g(n,S) \cong g(n)$.

The laser rate equations and the spin diffusion equation are solved with the objective of obtaining analytical forms of the threshold current and output polarization as a function of applied magnetic field. In solving these equations, we define a set of intermediate parameters. These are the spin polarization at any point $x(0 \le x \le x_1)$, $\Pi(x)$, the quantum dot spin polarization, $\Pi_s = (n^+ - n^-)/(n^+ - n^-)$, and the average barrier polarization, $\Pi_{s,b} = (n_b^+ - n_b^-)/(n_b^+ - n_b^-)$, where $n_b^{\pm}$ is the spin-up (spin-down) carrier density at the barrier. On the other hand the degree of circular polarization of the output, $\Pi_c = (S^+ - S^-)/(S^+ + S^-)$, and the light output $L = S^+ + S^-$ are measurable quantities, where $S^{\pm}$ are the density of the right- and left-circularly polarized photons. By solving the steady state laser rate equations [31] it can be easily shown that the barrier polarization and the output circular polarization are related to the carrier density through,

$$\frac{V_b}{V_{QD}}\frac{n_b}{\tau_{cap}} = v_g\left[g\left(n^+\right)S^- + g\left(n^-\right)S^+\right] + B_{sp}n^2 + Cn^3 \tag{3}$$

$$\frac{V_h}{V_{QD}}\frac{n_h^+ - n_h^-}{\tau_{cap}} = v_g\left[g\left(n^+\right)S^- - g\left(n^-\right)S^+\right] + \left(n^+ - n^-\right)\left(B_{sp}n + Cn^2 + \frac{2}{\tau_s}\right) \tag{4}$$

Similarly the output circular polarization is related to the carrier density through,

$$v_g\left[g\left(n^+\right)S^- + g\left(n^-\right)S^+\right] = \frac{S}{\Gamma\tau_{ph}} - \beta B_{sp}n^2 \tag{5}$$

$$v_g\left[g\left(n^+\right)S^- - g\left(n^-\right)S^+\right] = -\frac{S^+ - S^-}{\Gamma\tau_{ph}} - \beta B_{sp}n\left(n^+ - n^-\right) \tag{6}$$

Where $S^{\pm}$ are given by,

$$S^{\pm} = \frac{\Gamma\beta B_{sp}n^{\mp}n}{1/\tau_{ph} - \Gamma v_g g\left(n^{\mp}\right)} \tag{7}$$

Combining Eqns. 3 and 5, and noting that the pump current $I_{pump}=I_{th}$ when $n=n_{th}/(1 + \Pi_S)$ we get,

$$I_{th}(H) = qV_{QD}\left[\frac{1}{\Gamma}\frac{S_{th}}{\tau_{ph}} + \frac{B_{sp}n_{th}^2(1-\beta)}{(1+\Pi_s(H))^2} + \frac{Cn_{th}^3}{(1+\Pi_s(H))^3}\right] \tag{8}$$

where S_{th} is the photon density at threshold. It is found that the cumulative contribution from the terms containing threshold photon density (S_{th}) and the Auger recombination coefficient (C) in Eqn. (8) are less than 10 % of the contribution from the term having radiative recombination coefficient (B_{sp}), under all possible operating conditions of a spin laser. Hence, knowing $I_{th,0}$, the percentage threshold current reduction, $\Delta I_{th}(H)/I_{th,0}$ is reduced to a simplified form given by,

$$\frac{\Delta I_{th}(H)}{I_{th,0}} \cong \frac{\Pi_s(\Pi_s + 2)}{(1+\Pi_s)^2} \tag{9}$$

It is of interest to note that this parameter is determined exclusively by Π_S.
Similarly, the output polarization (as obtained by using Eqn. 7 and Eqns. 5 and 6) is given by,

$$\frac{\Pi_c\left(H, I_{pump}\right)}{\Pi_s} = -\frac{1 + \Gamma v_g\tau_{ph}\dfrac{dg}{dn}n_{tr}}{1 + \Gamma v_g\tau_{ph}\dfrac{dg}{dn}n_{tr} - \Gamma v_g\tau_{ph}\dfrac{dg}{dn}n_{th}\left(1-\Pi_s\right)} \tag{10}$$

We also define a gain anisotropy parameter,

$$g_A\left(H, I_{pump}\right) = \frac{g\left(n^+\right)}{g\left(n^-\right)} \cong \frac{1+\Pi_s}{1-\Pi_s} \tag{11}$$

The parameters ($\Delta I_{th}/I_{th,0}$), g_A, Π_c, and $d\Pi_c/d(I_{th}/I_{th,0})$ are plotted against injection current and applied magnetic field and are depicted in Figs. 3 and 4. The device and material parameters used and obtained from our own work and from recent reports [32-35].

Measurements have been carried out on spin-polarized quantum dot VCSELs. In particular we have measured the reduction in the threshold current due to spin injection of electrons and the electrical modulation of the output polarization. We also choose an operating temperature of 200 K, which is low enough to allow enough spin polarized electrons to reach the QD active region from the MnAs Schottky tunnel contact. The laser heterostructure shown in Fig. 1 is grown by MBE.

The lasers were mounted in a magneto-optical cryostat for measurements, which were done in the Faraday geometry. All measurements reported here were carried out on 15 μm diameter VCSELs at the design temperature of 200 K where no offset exists between the photoluminescence gain peak and the distributed Bragg reflector (DBR) reflectivity peak and hence lasing with the minimum threshold current is obtained. This temperature is carefully

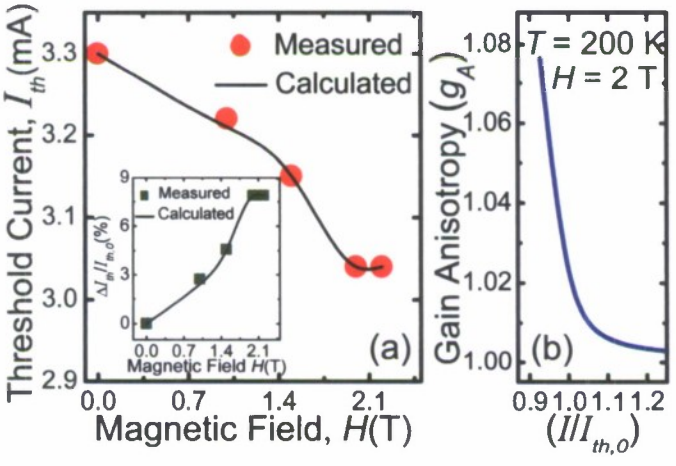

Figure 3 : Data from 15 μm diameter InAs/GaAs QD spin VCSEL at 200 K: (a) calculated and measured reduction of threshold current with magnetic field applied perpendicular (hard axis) to the plane of the MnAs contact. The inset shows the calculated and measured percentage reduction of threshold current with field; (b) calculated variation of gain anisotropy parameter, as defined in Eqn. (7.9) (text) with normalized pump current.

chosen such that a large number of spin-polarized carriers can still reach the QD active region. The current biasing to the lasers was in the continuous wave mode. The measured reduction and percentage reduction ($\Delta I_{th}/I_{th,0}$) of the threshold current with application of magnetic field are plotted in Fig. 3(a) and its inset and there is good agreement with the calculated values of the respective parameters. A maximum threshold current reduction ($\Delta I_{th}/I_{th,0}$) of ~8% is measured at H = 2.1 T, at which field the saturation of the out-of-plane magnetization of MnAs contact also occurs. No threshold reduction is observed for the non-magnetic VCSEL. The calculated variation of gain anisotropy with current (Fig. 3(b)) indicates that spin related phenomena are operative only for lasers biased near threshold, $I_{th,0}$. It may be noted that the gain anisotropy (g_A) is largest just below threshold. This is easily understood by considering injection of spin polarized carriers in a laser biased slightly below threshold, $I_{th,0}$. An application of magnetic field results in injection of spin polarized carriers which can preferentially enhance the gain of one polarization mode above threshold gain, while the gain of the other polarization mode still remains sub-threshold, resulting in a large gain anisotropy and reduction in the threshold current. As the injection is increased, the difference in peak gain of the two polarization modes will decrease and the gain anisotropy will also steadily decrease. The maximum value of g_A attainable with ferromagnetic MnAs spin injector is ~ 2, under the ideal conditions of negligible spin flip during transport of spin-polarized carriers to the active region. An increase in spin

injection efficiency will lead to higher gain anisotropy (Eq. 11) and hence enhanced threshold reduction and output circular polarization.

The output polarization characteristics of the spin laser are discussed next. For a fixed bias current, the measured value of Π_c as a function of the applied magnetic field follows the measured out-of-plane magnetization of the MnAs contact very closely. In comparison the observed polarization of the non-magnetic VCSEL is negligible. The modulation of the output polarization Π_c with bias current was measured at different saturation magnetic fields and the data are shown in Fig. 4(a). As the pump current reaches threshold, the carrier concentration of the polarized lasing mode with higher gain (say S^+) becomes clamped at n_{th}. Further increase in pump current will increase the carrier concentration of the mode with lower gain (S^-), till n_{th} is reached for this mode also and the mode will lase. It is easily seen that the spin polarization in the QD active region will steadily decrease as the injection increases beyond the point where

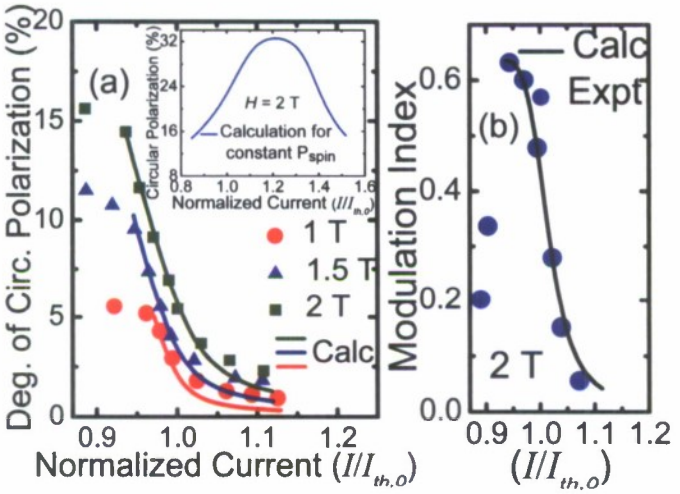

Figure 4: (a) Calculated and measured modulation of output circular polarization of InAs/GaAs QD spin VCSEL as a function of normalized pump current at different magnetic fields. The inset shows calculated polarization for *constant* pump current spin polarization, instead of the variation of P_{spin} shown in Fig. 7.2; (b) measured modulation index versus pump current. The calculated values are shown for currents at and above threshold.

the first threshold (for S^+) is reached. Intuitively, it is expected that in the injection regime between the thresholds for S^+ and S^-, the output polarization will steadily increase and then decrease after the threshold for S^- is crossed. However, considering the transport of injected spin-polarized carriers from the ferromagnetic contact to the active region by spin diffusion, and the steady decrease of the spin polarization in the active (gain) region after the threshold of S^+ is reached, the pump spin polarization P_{spin} also decreases, as illustrated in Fig. 2. This leads to a decrease in output circular polarization as soon as the pump current increases beyond the threshold (for S^+). Thus the intuitive picture of the variation of output polarization would be valid only if diffusive transport of injected carriers is neglected and P_{spin} is held constant (inset to Fig. 4(a)). This is the first demonstration of electrical modulation of the output polarization of a semiconductor laser. We define a modulation index as $\Delta\Pi_c/\Delta(I/I_{th})$ and this parameter is plotted in Fig. 4(b) as a function of normalized current along with the calculated data. The index goes through a maximum value of 0.6 at $I/I_{th,0} \cong 1$ and decreases rapidly for high bias currents due to significant reduction of gain anisotropy in this range.

1.5 Reference

[1] S. Hallstein et al., Phys. Rev. B 56, R7076 (1997).
[2] H. Ando, T. Sogawa, and H. Gotoh, Appl. Phys. Lett. 73, 566 (1998).
[3] J. Rudolph et al., Appl. Phys. Lett. 82, 4516 (2003).
[4] Optical Orientation, edited by F. Meier and B. P. Zakharchenya (Elsevier Science, Amsterdam, 1984).
[5] M. San Miguel, Q. Feng, and J. V. Moloney, Phys. Rev. A 52, 1728 (1995).
[6] J. Rudolph et al., Appl. Phys. Lett. 87, 241117 (2005).
[7] M. Holub et al., Appl. Phys. Lett. 87, 091108 (2005); also see associated comment and reply.
[8] A. T. Hanbicki et al., Appl. Phys. Lett. 80, 1240 (2002).
[9] J. Martin-Regalado et al., IEEE J. Quantum Electron. 33, 765 (1997).
[10] A. K. J. van Doorn, et.al Appl. Phys. Lett. 69, 1041 (1996).
[11] See EPAPS Document No. E-PRLTAO-98-057715. For more information on EPAPS, see http://www.aip.org/pubservs/epaps.html.
[12] M. Beck et al., Europhys. Lett. 75, 597 (2006).
[13] S. A. Crooker and D. L. Smith, Phys. Rev. Lett. 94, 236601 (2005).
[14] R. Nagarajan et al., IEEE J. Quantum Electron. 28, 1990 (1992).
[15] L. V. Dao et al., Appl. Phys. Lett. 73, 3408 (1998).
[16] K. Jarasiunas et al., Semicond. Sci. Technol. 19, S339 (2004).
[17] K. Morita et al., Physica (Amsterdam) E21, 1007 (2004).
[18] B. Dareys et al., J. Phys. IV 3, 351 (1993).
[19] L. F. Lester et al., Appl. Phys. Lett. 59, 1162 (1991).
[20] A. F. G. Monte et al., J. Appl. Phys. 85, 2866 (1999).
[21] S. Hausser et al., Appl. Phys. Lett. 56, 913 (1990).
[22] R. J. Ram et al., IEEE Photonics Technol. Lett. 8, 599 (1996).
[23] B. J. Thibeault et al., J. Appl. Phys. 78, 5871 (1995)
[24] M. Holub et al., Phys. Rev. Lett. 98, 146603 (2007).
[25] D'yakonov, M. I., and V. I. Perel', Sov. Phys. Solid State 13, 3023 (1971).
[26] Z. G. Yu and M. E. Flatté, Phys. Rev. B 66, 201202 (2002).
[27] D. Basu et al., Appl. Phys. Lett. 92, 091119 (2008).
[28] R. P. Panguluri et al., Phys. Rev. B 68 201307(R) (2003).
[29] D. Saha, M. Holub, P. Bhattacharya, and Y. C. Liao, Appl. Phys. Lett. 89, 142504 (2006).
[30] M. San Miguel, Q. Feng, and J. V. Moloney, Phys. Rev. A 52, 1728 (1995).
[31] See EPAPS Document No. E-PRLTAO-102-006912 for derivation of all the analytical expressions for a spin laser. For more information on EPAPS see, http://www.aip.org/pubservs/epaps.html (2008).
[32] N. Kirstaedter et al., Appl. Phys. Lett. 69, 1226 (1996).
[33] S. Ghosh et al., Appl. Phys. Lett. 79, 722 (2001).
[34] Igor Žutić, Jaroslav Fabian, and S. Das Sarma, Rev. Mod. Phys. 76, 323 (2004).
[35] R. Ram et al., IEEE Photonics Technol. Lett. 8,599 (1996).

2. Amplification of Spin-Current Polarization

Comprehensive Summary of the significant work accomplished

Electrical injection and control of large spin polarization in semiconductors are indispensable for the realization of useful spintronic devices. [1-3] Electrical spin injection has been demonstrated in all-metal devices,[4,5] ferromagnet/semiconductor based lateral spin-valves, and also electrically injected spin-polarized lasers.[6-8] Despite these advances, achievement of current spin polarizations of 100%, or more, and electrical control of such polarizations have remained elusive. An electrically controlled spin-current amplifier is a desirable solution to this problem. Theoretical proposals for such devices have been made,[9-16] but experimental demonstration is lacking. Here we propose and demonstrate a novel electrically controlled three terminal spin-polarization amplifier using a dual-drain lateral spin-valve configuration, which can provide large current spin polarization for both majority and minority spins, independent of the injected (source) polarization. The device amplifies the small injected polarization in a semiconductor channel to a large value, which can be extracted at the second drain contact. The sign and mag-nitude of the amplifier gain can be controlled both at the input and output terminals to achieve a desired polarization. The device also generates a pure spin-current with zero charge current. This aspect can be used to envisage a new class of spintronic devices.

When a current flows in a ferromagnet/semiconductor/ferromagnet lateral spin-valve, the electrochemical potentials of spin-up ($\mu\uparrow$) and spin-down ($\mu\downarrow$) electrons split in the semiconductor channel. The splitting ($\Delta\mu = \mu\uparrow - \mu\downarrow$) depends on the relative directions of magnetization of the two ferromagnetic contacts. It is large when the two contacts (we call them source and drain1) are magnetized in opposite directions, and small (with a crossover in the center) when the contacts are magnetized in the same direction. If a point contact (drain2) is then placed at the center of the semiconductor channel (L_{chan}) of the spin-valve with anti-parallel magnetization of source and drain1 contacts, its potential can be varied between $\mu\uparrow$ and $\mu\downarrow$, enabling a controlled collection of spin-up and spin-down electrons. It is important to note that the two spin-currents flow in opposite directions and the current polarization can be controlled by varying the drain2 bias. It is necessary to ensure that the drain2 contact acts as a high-impedance probe, so as to minimize any perturbation of the channel potentials.

Most significant advancements and Conclusions (include equations & figures as appropriate)

A simple two-channel model for the spin-current amplifier is shown in Fig. 1(a) The source and drain1 ferromagnetic contacts are magnetized in opposite directions. The spin-up (spin-down) conductivities of the ferromagnet and the tunnel barrier are shown as $R_{\uparrow F}$ ($R_{\downarrow F}$) and $R_{\uparrow TB}$ ($R_{\downarrow TB}$), respectively. The resistance of the semi-conductor channel is R_n. The ideal drain2 point contact is at the center of the semi-conductor channel. The electrochemical potentials for spin-up ($\mu\uparrow$) and spin-down ($\mu\downarrow$) electrons are split at x = 0. The drain2 voltage V_{D2} can be varied between $\mu\uparrow$ and $\mu\downarrow$ enabling a controlled collection of spin-up and spin-down electrons. The two spin-currents $I_{D2\uparrow}$ and $I_{D2\downarrow}$ can flow in opposite directions depending upon the value of V_{D2}, yielding spin polarization gain greater than unity.

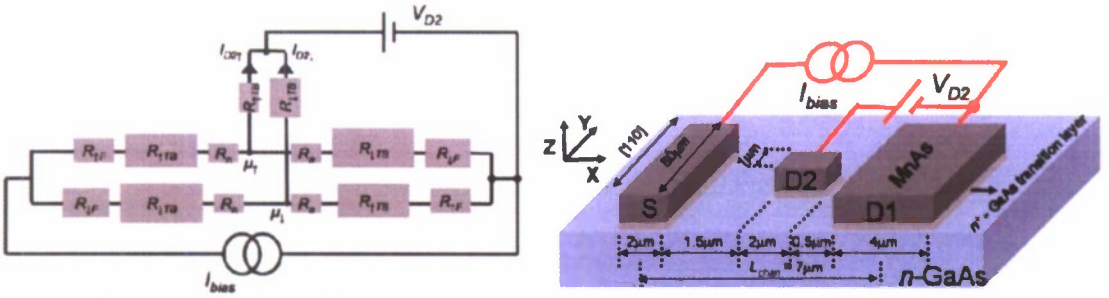

Figure 1: (a) The two-channel model for the spin polarization amplifier, which is a dual-drain lateral spin-valve. The polarizer and analyzer are magnetized in opposite directions. (b) Schematic diagram of a spin polarization amplifier (not to scale). All three contacts S, D1 and D2 have magnetic easy axes along the ˆy direction (GaAs [011] direction). The center of contact pad D2 is also the center of the effective channel L_{chan}. A fixed current bias I_{bias} establishes the spin-up and spin-down electrochemical potentials in the channel. The drain2 voltage V_{D2} controls the spin-current in contact pad D2.

A schematic of the typical dual-drain lateral spin-valve is shown in Fig. 1(b). The ferromagnetic source contact (S) injects a spin-polarized current into the non-magnetic channel through a Schottky tunnel barrier,[16-17] which is collected at one of two ferromagnetic drain contacts (D1 and D2). The contact D2 is, however, distributive in nature (compared to the ideal point contact) and exactly centered within the effective channel between S and D1. The D2 terminal is operated near zero-bias with respect to the channel potential and the contact pad area is made much smaller than that of S and D1. Such operating conditions and pad dimensions ensure that the current collected at D2 is very small, compared to that collected at D1, and the potential in the channel is primarily determined by the current bias (I_{bias}) between S and D1. The geometric aspect ratios for S, D1 and D2 are chosen appropriately such that the coercivity is the largest for S and the smallest for D2. This particular choice allows various magnetization alignment conditions between S, D1 and D2 to be realized by sweeping the magnetic field B.

Figure 2 schematically shows the relative orientation of magnetization in S, D1 and D2 as B is swept from a large negative (positive) to a large positive (negative) value. The distinct states of magnetizations (M1-M4) and the corresponding D2 current (I_{D2}) are also shown for the -B to +B sweep. When the magnetic field is largely negative, S, D1 and D2 are all aligned in the same direction as B (state M1). The contacts D2 (state M2) , D1 (state M3) and S (state M4) then flip, in that sequence, as the magnetic field sweeps through zero in the positive direction because of the relative magnitude of the coercivities. If a bias current (I_{bias}) is applied between S and D1 having parallel magnetizations, it can be shown by solving the coupled spin drift-diffusion equations [16, 18-20] that the electrochemical potentials for spin-up ($\mu\uparrow$) and spin-down ($\mu\downarrow$) electrons in the channel are split. Higher doping in the channel and low current bias (hence, low electric field) operation in our devices ensure that drift is negligible.[21] In absence of drift, it can be shown that the electrochemical potential splitting is antisymmetric with respect to the center, $x = L_{chan}/2$,which is also the center of contact pad D2. Hence, a bias voltage equal to the cross-over potential for spin-up and spin-down electrons in the channel can be applied at D2 ($V_{D2} = V_{null}$) to make current $I_{D2} = 0$ for states M1, M2 and M4 in Fig. 2. Under this condition, spin up ($I_{D2}\uparrow$) and spin-down ($I_{D2}\downarrow$) currents are both equal to zero. However, I_{D2} will be non-zero under the same bias condition for state M3 where S and D1 are anti-parallel, for which the electrochemical potentials $\mu\uparrow$ and $\mu\downarrow$ are split at $x = 0$. The current spin polarization

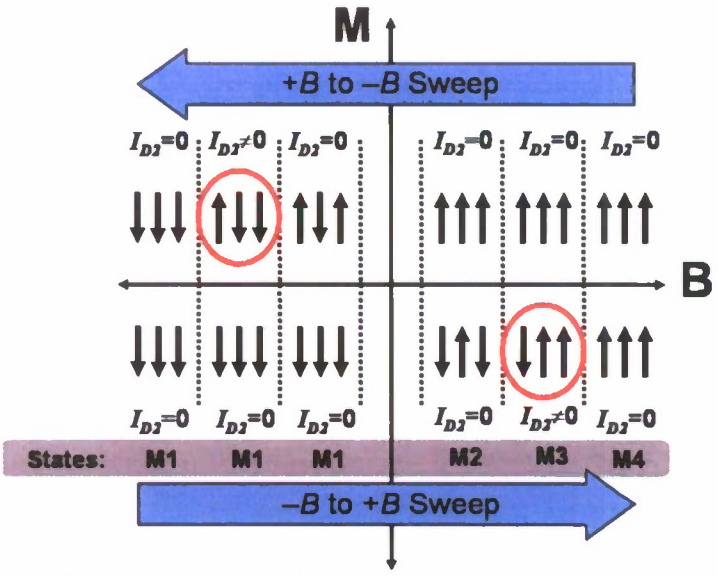

Figure 2: The magnetization direetions of the three ferromagnetie eontaet pads S, D1 and D2 as the magnetie field B is swept in both direetions. Eaeh group of three arrows (left to right) represents the magnetization direetions of S, D2 and D1 contaet pads, respectively. The distinct states of magnetizations M1-M4 and the eorresponding I_{D2} values for each state are shown for -B to +B sweep. A non-zero drain2 current I_{D2} flows in state M3.

is conventionally defined [16-19, 22] as $\alpha_{D2} = I_{D2,spin}/I_{D2,charge}=(I_{D2\uparrow} - I_{D2\downarrow})/(I_{D2\uparrow} + I_{D2\downarrow})$. Thus the current spin polarization at the D2 terminal can be much larger than that of the channel, resulting in a spin-current gain in the system. For a fixed I_{bias} in state M3, V_{D2} can be varied to control the spin polarization gain (amplification). The gain can also be controlled with $V_{D2} = V_{null}$ and variable I_{bias}. It may be noted that the design of the device facilitates lateral diffusion to compensate for any decrease in $\Delta\mu$ in the channel due to carrier extraction at D2.

In our experiment, we fabricate dual-drain lateral spin-valves from a ferromagnetic Manganese Arsenide (MnAs) (90 nm thick), n^+ -doped (~ 10^{18}-10^{19} cm^{-3}) Gallium Arsenide (GaAs) transition layer and n-doped GaAs ($N_D = 10^{17}$ cm^{-3}) heterostructure, [8,23] which is grown by MBE on a semi-insulating (SI) (001) GaAs substrate. The n-doping profile in the GaAs channel region and the GaAs/MnAs transition layer is shown in Fig. 3(a). The S, D1 and D2 contacts are made ferromagnetic by patterning them on MnAs. The source contact injects spin-polarized electrons through the heavily doped spin-selective Schottky tunnel barrier into the n -doped GaAs channel, which are subsequently collected at D1 or D2 through an identical tunnel barrier. The presence of a tunnel barrier is confirmed from temperature dependent conductivity measurement. Eight devices with different channel lengths (L_{chan}) and aspect ratios for the contacts pads were fabricated. The D2 pad is centered within the channel in all the devices. It is observed that the devices with smaller channel lengths give a larger spin-current amplification. Devices with aspect ratios different from those reported here exhibit exactly the same be-havior, except the response is observed at a different magnetic field due to their different contact coercivities. The device shown in Fig. 2 is fabricated as follows. In the first step, the channel is defined on n -doped GaAs by etching away MnAs and n^+ -doped GaAs layers leaving only the S (L × W = 50 μm × 2 μm), D1 (L ×W = 50 μm × 4 μm) and D2 pads (L ×W =1 μm × 2 μm).

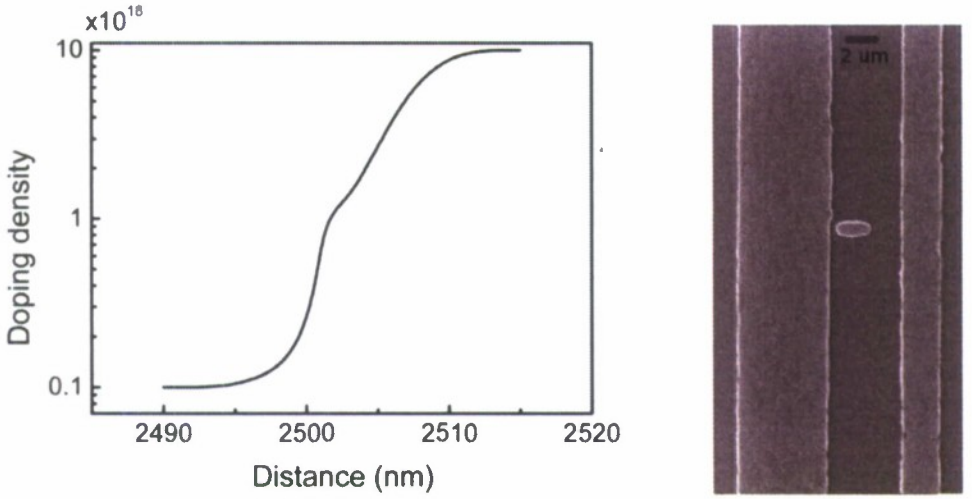

Figure 3: (a) Doping profile in the GaAs channel and GaAs/MnAs transition layer. The zero of the x-axis is the top surface of the semi-insulating GaAs (001) substrate. This confirms the graded doping and the heavily doped GaAs region beneath MnAs, necessary for the Schottky tunnel contact. (b) An SEM image of the spin-current amplifier after delineating source, drain1 and drain2 contacts by wet etching.

Next, silicon dioxide (SiO_2) is deposited as a passivation layer and via holes are created by dry etching. Finally, Ti/Au metal is evaporated by PVD and contacts are formed in a lift-off. process. An SEM image of the device is shown in Fig. 3(b). The spin-selectivity of the MnAs/GaAs tunnel barrier conductance, $\beta = G\uparrow/G\downarrow$ is determined to be 1.9 from channel length dependent magnetoresistance measurements on MnAs/GaAs/MnAs lateral spin-valves. The conductivity of the n -doped GaAs channel (σ_n) is four orders of magnitude lower than that of MnAs (σ_f) in the temperature range of operation of our devices. Identical control devices with non-magnetic D2 were also fabricated and characterized.

The device operation is based on a spin-valve with source and drain1 magnetized in opposite directions. The magnetoresistance measurement is done to ensure basic spin-valve behavior in these devices. Figure 4 shows the measured magnetoresistance as a function of magnetic field at 10 K (circles). The drain2 current of a spin-current amplifier is also shown alongside (squares). The peak values are normalized to unity. The resistance is low when source and drain1 are magnetized in the same direction at high magnetic fields. The magnetoresistance is high when they are magnetized in opposite directions (H =1.5 kOe). This confirms the basic spin-valve characteristics in these devices. The anti-parallel configuration for spin-current amplifiers can therefore be achieved at H = 1.5 kOe. The complete overlap between the magnetoresistance and the drain2 current confirms that the peak I_{D2} coincides with the peak anti-parallel alignment between S and D1. Control experiments were also done to ensure spin-dependency of the observed effects.

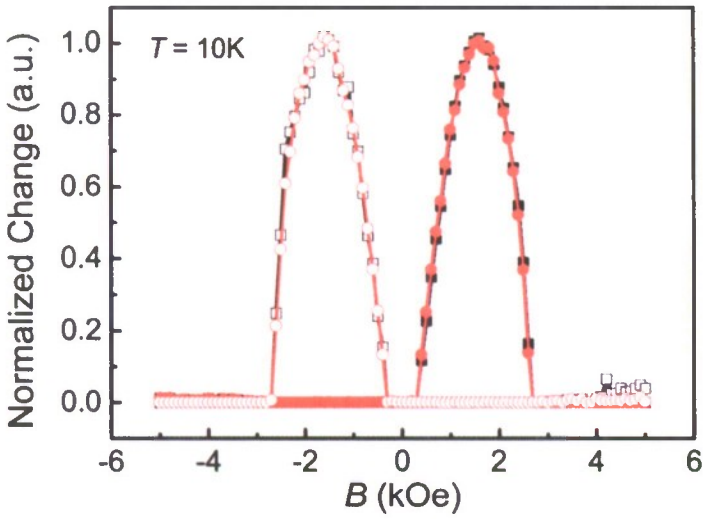

Figure 4: The magnetoresistance of a MnAs/GaAs lateral non-local spin-valve (circles) and drain2 current ID2 of a spin polarization ampli.er (squares) as a function of applied magnetic field B at 10 K. The filled (open) symbols correspond to -B to +B (+B to -B) sweep. The polarizer and analyzer dimensions of the MnAs/GaAs lateral spin-valve are same as that of S and D1 contact pads of the spin polarization amplifier, respectively. The peak values are normalized to unity. The overlap confirms that the peak I_{D2} coincides with the peak anti-parallel alignment between S and D1.

The spin-current amplifier characteristics are measured by mounting the samples in a cryostat placed between the poles of an electromagnet. Figures 5(a) and (b) show current I_{D2} measured as a function of in-plane magnetic field B (directed along the y axis) for different temperatures T (I_{bias} = 100 μA) and I_{bias} (T = 10 K), respectively. The voltage V_{D2} is set to the corresponding null voltages (V_{null}, which depends on T and I_{bias}) in each case. A typical value for V_{null} at 10 K and I_{bias} = 100 μA is ~21 mV. The peak of I_{D2} coincides with the peak anti-parallel alignment between S and D1 at B = 1.5 kOe, which corresponds to state M3 in Fig. 3. The sign of current I_{D2} changes when the roles of S and D1 are reversed for the same value of B. This indicates that $\Delta\mu$ (= $\mu\uparrow$ - $\mu\downarrow$) and spin dependency of the effect change sign. The current decreases with increasing T and decreasing I_{bias}. Magnetoresistance measurements with conventional and non-local spin-valves show a peak at the same value of B, which also confirms that I_{D2} is sensitive to the spin-degree of freedom only. No response is observed for the control devices, with a non-magnetic D2 contact pad.

The experimental observations are explained by invoking the spin-diffusion model. The electrochemical potential in the channel region is described by the spin-diffusion equation as

$$\frac{\partial^2(\mu_\uparrow - \mu_\downarrow)}{\partial x^2} = \frac{\mu_\uparrow - \mu_\downarrow}{\lambda_{sf}^2} \qquad (1)$$

where λ_{sf} is the spin-diffusion length in the channel region. The small contribution from spin-drift is neglected because of the high doping in the channel region.

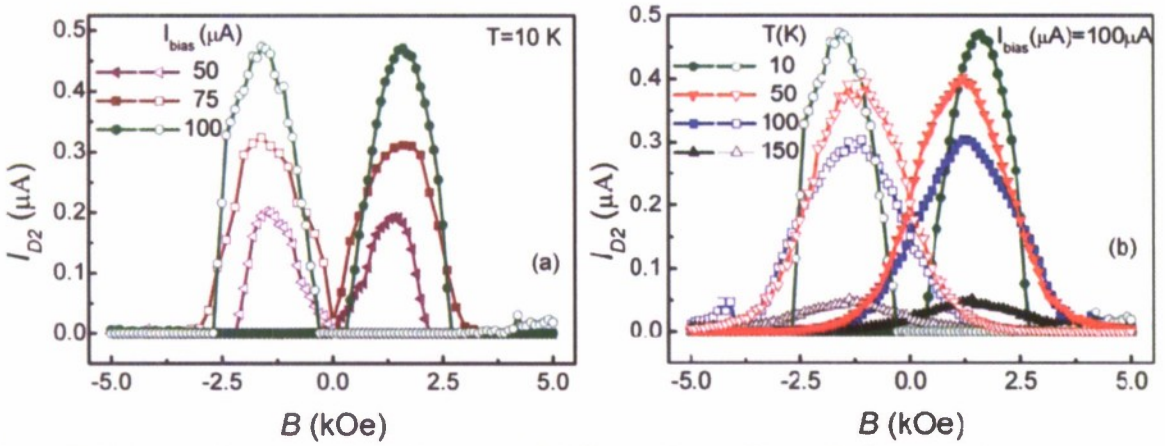

Figure 5: (a) Current I_{D2} as a function of magnetic field B for different Ibias with V_{D2} set to their corresponding null values (V_{null}) at 10 K; (b) current I_{D2} as a function of magnetic field B for different temperatures T with I_{bias}=100 μA and $V_{D2} = V_{null}$. The filled (open) symbols corresponds to −B to +B (+B to −B) sweep.

The above equation is solved with the boundary conditions that the spin-currents are continuous at x = 0 and x = L_{chan} (assuming there is no spin-flip scattering at the interface) as given by,

$$j_{\uparrow}(0^-) = G_{\uparrow}\,[\mu_{\uparrow}(0^+) - \mu_{\uparrow}(0^-)] \quad (2)$$

$$j_{\downarrow}(0^-) = G_{\downarrow}\,[\mu_{\downarrow}(0^+) - \mu_{\downarrow}(0^-)] \quad (3)$$

$$j_{\uparrow}(0^-) - j_{\downarrow}(0^-) = j_{\uparrow}(0^+) - j_{\downarrow}(0^+) \quad (4)$$

where the current in each spin-channel is calculated as,

$$j_{\uparrow(\downarrow)} = \frac{\sigma_{\uparrow(\downarrow)}}{e}\frac{\partial \mu_{\uparrow(\downarrow)}}{\partial x} \quad (5)$$

These equations are also written for x = L_{chan}. The solution of the spin-diffusion equation for the spin-up and spin-down electrons in S and D1 lateral MnAs/GaAs/MnAs spin-valves yields the electrochemical potentials in the channel as,

$$\mu_{\uparrow(\downarrow)} = \frac{jxe}{\sigma_n} + (-)\frac{2K}{\sigma_n}\left[\gamma exp\left(-\frac{x}{\lambda_{sf}}\right) + exp\left(-\frac{x - L_{chan}}{\lambda_{sf}}\right)\right] \quad (6)$$

where j is the current density in the channel, e is the electron charge, and γ is +1 (-1) when magnetizations of S and D1 are anti-parallel (parallel). The constant K is determined from the boundary conditions as:

$$K = \frac{je\sigma_n}{8}\left[\frac{1+\alpha_f}{G_{\uparrow}} - \frac{1-\alpha_f}{G_{\downarrow}}\right] \Big/ \left[\gamma + exp\left(-\frac{L_{chan}}{\lambda_{sf}}\right)\right] \quad (7)$$

where α_f (~ 0.5) is the spin polarization of MnAs[26]. The current I_{D2} is then obtained as:

$$I_{D2} = \int_{L1}^{L2}\left[G_{\uparrow}\left(V_{D2} - \frac{\mu_{\uparrow}}{e}\right) + G_{\downarrow}\left(V_{D2} - \frac{\mu_{\downarrow}}{e}\right)\right] W_{D2}\,dx \quad (8)$$

where L1 are L2 are the bounding x coordinates of contact pad D2.

Figure 6(a) shows the measured peak I_{D2} as a function of I_{bias} in state M5 of the device. Theoretically calculated values of peak I_{D2}, using Eqn. 7 and a value of λ_{sf} =7 μm, are also shown alongside the measured data. Figure 6(b) shows the estimated spin-diffusion length as a function of temperature. The good agreement provides further evidence for the spin-dependent effects in these devices. The electrochemical potential difference between spin-up

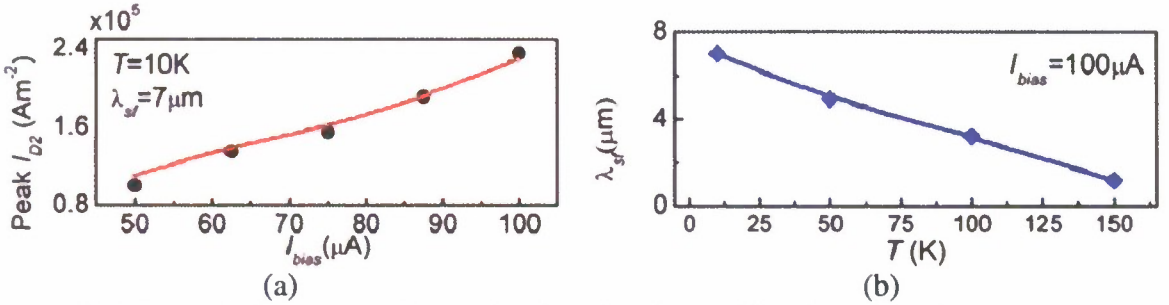

Figure 6: (a) The peak drain2 current I_{D2} as a funetion of I_{bias} in state M3. The solid eireles represent measured data at 10 K and the solid line represents the theoretieally ealculated values based on Eqn. 3.8. The spin diffusion length λ_{sf} is found to be 7 μm at 10 K. The spin-up and spin-down currents flow in opposite directions in contact pad D2, yielding spin polarization gain greater than unity; (b) estimated spin diffusion length as a function of temperature.

and spin-down electrons is plotted as a function of position along the channel in Fig. 7. $\mu_\uparrow$ and $\mu_\downarrow$ remain anti-symmetric in the channel, making I_{D2} zero for all T and I_{bias} with $V_{D2} = V_{null}$, when magnetizations of S and D1 are parallel.

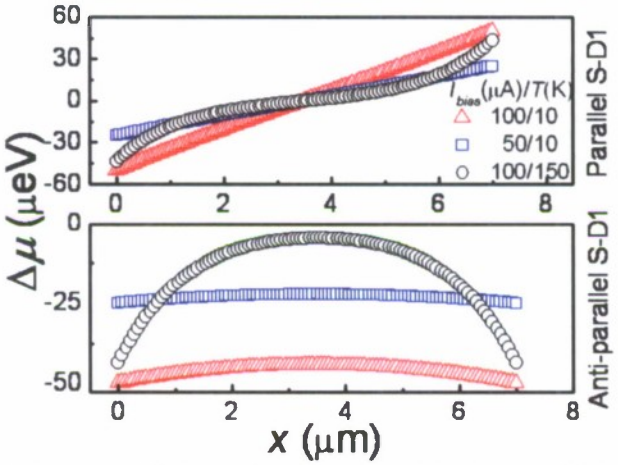

Figure 7: The anti-symmetric (symmetrie) electrochemieal potential differenee (Δμ) between spin-up and spin-down eleetrons in the ehannel when S and D1 eontaet magnetizations are parallel (anti-parallel) for two different temperatures T and I_{bias}. Δμ decreases in the channel at higher temperature due to enhaneed spin relaxation. It inereases at the souree/ehannel interfaee (x = 0) for higher I_{bias} due to enhanced spin-splitting.

On the other hand, when the magnetizations of S and D1 are antiparallel, the difference Δμ decreases with decreasing I_{bias} and increasing T, which results in reduced I_{D2} in spite of increased tunnel conductance at higher T .

We calculate the current spin polarization α_{D2} as a function of I_{bias} and V_{D2} from measured values of I_{D2}. Figure 8(a) shows the current spin polarization gain (α_{D2}/α_f) as a function of V_{D2} for different I_{bias}. The voltage V_{D2} is varied in steps of 5 μV for the measurement of I_{D2} in this case. The gain curve shifts along the V_{D2} axis with increasing I_{bias} due to the increasing value of V_{null}. Figure 8(b) shows the gain curves as a function I_{bias} for different values of V_{D2}. The current I_{bias} is varied in steps of 0.5 μA during this measurement. The plots show that

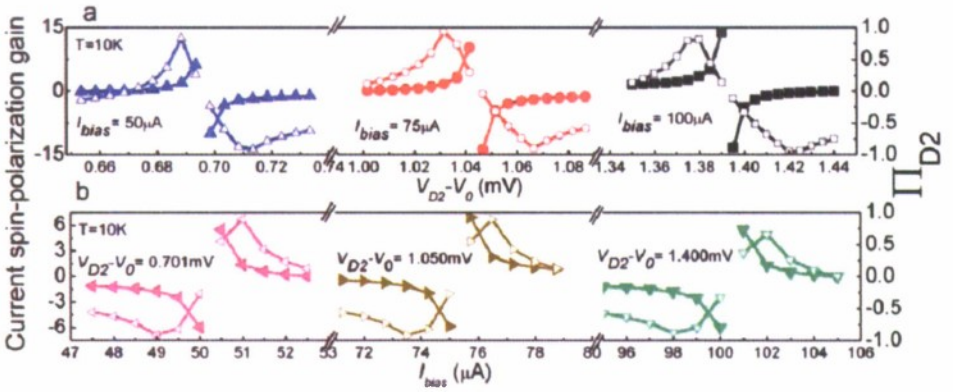

Figure 8: Dual control of the spin polarization gain. The open (closed) symbols represent nega-tive (positive) gain. (a) Spin polarization gain as a function of V_{D2} for varying I_{bias} at 10 K. The gain increases with increasing I_{bias}; (b) spin polarization gain as a function of I_{bias} for varying V_{D2} at 10 K. A constant offset voltage, V_0 = 19.565 mV is subtracted from each of the V_{D2} values. The gain curves exhibit singularities along the V_{D2} and I_{bias} axes when a pure spin-current flows through contact pad D2 (I_{D2} = 0).

the magnitude and sign of the polarization gain can be varied by changing the value of I_{bias}. The gain curves exhibit several singularities along the V_{D2} and I_{bias} axes. These occur when the charge current at D2, I_{D2}=0 ($I_{D2\uparrow}$ =-$I_{D2\downarrow}$) and a pure spin current, I_{spin} (=$I_{D2\uparrow}$ -$I_{D2\downarrow}$) flows through this contact. [12,14] The peak gain that can be measured is limited by the smallest possible increment of V_{D2} and I_{bias} around these singularities. Hence, a combination of V_{D2} and I_{bias} can be used to electrically control the spin polarization gain. The gain can be made negative or positive by external bias, independent of the polarization of S and D1.

References:

[1] S. A. Wolf, *et. al.* Science **294**, 1488 (2001).
[2] D. D. Awschalom and M. E. Flatté, Nat. Phys. 3, 153 (2007).
[3] I. Žutić, J. Fabian, and S. D. Sarma, Rev. Mod. Phys. 76, 323 (2004).
[4] M. Johnson and R. H. Silsbee, Phys. Rev. Lett. 55, 1790 (1985).
[5] F. J. Jedema, A. T. Filip, and B. J. van Wees, Nature (London) 410, 345 (2001).
[6] I. Appelbaum, B. Huang, and D. J. Monsma, Nature (London) 447, 295 (2007).
[7] P. R. Hammar and M. Johnson, Phys. Rev. Lett. 88, 066806 (2002).
[8] D. Saha, M. Holub, P. Bhattacharya, and Y. C. Liao, Appl. Phys. Lett. 89,142504 (2006).
[9] S. Datta and B. Das, Appl. Phys. Lett. 56, 665 (1990).
[10] W. Long, Q.-F. Sun, H. Guo, and J. Wang, Appl. Phys. Lett. 83, 1397 (2003).
[11] J. Wang, K. S. Chan, and D. Y. Xing, Phys. Rev. B 72, 115311 (2005).
[12] H. Dery, L. Cywinski, and L. J. Sham, Phys. Rev. B 73, 161307 (2006).
[13] S.-W. Jung and H.-W. Lee, Phys. Rev. B 73, 165302 (2006).
[14] C. Benjamin and R. Citro, Phys. Rev. B 72, 085340 (2005).
[15] J. Fabian and I. Žutić, Phys. Rev. B 69, 115314 (2004).
[16] E. I. Rashba, Phys. Rev. B 62, R16267 (2000).
[17] G. Schmidt, *et.al*, Phys. Rev. B 62, R4790 (2000).
[18] I. Žutić, J. Fabian, and S. Das Sarma, Phys. Rev. Lett. 88, 066603 (2002).
[19] Z. G. Yu and M. E. Flatté, Phys. Rev. B 66, 235302 (2002).
[20] P. C. van Son, H. van Kempen, and P. Wyder, Phys. Rev. Lett. 58, 2271 (1987).
[21] R. I. Dzhioev, *et.al*, Phys. Rev. B 66, 245204 (2002).
[22] Z. G. Yu and M. E. Flatté, Phys. Rev. B 66, 201202 (2002).
[23] A. T. Hanbicki, *et.al*, Appl. Phys. Lett. 82, 4092 (2003).
[24] X. Lou, *et.al*, Nat. Phys. 3,197 (2007).
[25] S. Garzon, I. Žutić, and R. A. Webb, Phys. Rev. Lett. 94, 176601 (2005).
[26] R. P. Panguluri, *et.al*, Phys. Rev. B 68, 201307 (2003).

3. Electrically Driven Spin-Dynamics of Paramagnetic Impurities: A Spin Capacitor

Comprehensive Summary of the significant work accomplished

Electrical spin injection, manipulation and detection in non-magnetic materi-als have gained interest in recent years for the possibility of realizing spintronic devices [1]. The successful operation of spin-valve and spin-torque devices [2-6] is dependent on minimizing spin-scattering during transport through non-magnetic metals, semiconductors and hetero-interfaces [7]. In contrast, in this paper we report experiments on a lateral MnAs/GaAs/MnAs spin-valve structure (Fig.1) [8,9] with paramagnetic Mn impurities that are deliberately in-troduced into the channel region. These Mn impurities cause spin-flip

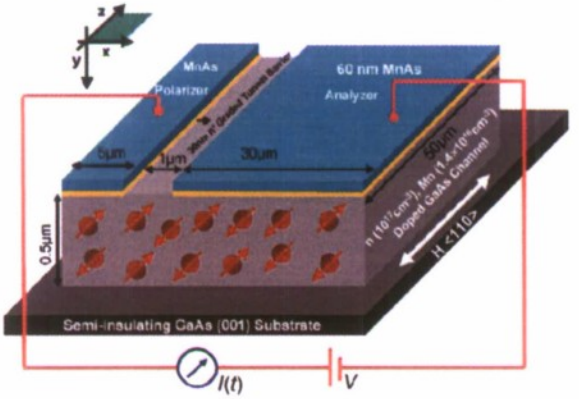

Figure 1: Schematic cross-section (not to scale) of a typical Mn-doped spin-valve. The channel region is n-type and it is lightly co-doped with Mn impurities. The arrows indicate the initial unpolarized Mn impurities.

scattering and, since they do not have any significant alternative means of relaxation [10], get polarized in the process resulting in a decrease in the spin-flip current and hence the terminal current. This transient response in the terminal current due to an electrically driven impurity polarization is the subject of the present study. The study demonstrates electrical detection and manipulation of the spin-magnetic moment of bound magnetic impurities in semiconductors, which may be useful in envisioning new devices [11]. The observed phenomenon should be scalable to very few magnetic impurities, which will be useful for the realization of quantum information processing devices. The study also provides an easy method to determine the spin-spin scat-tering time constant between various magnetic impurities and delocalized conduction electrons.

We demonstrate experimentally, for the first time to our knowledge, that (1) the impurities can be polarized when the spin-valve is operated in the anti-parallel configuration but not in the parallel configuration, and, (2) this polarization leads to a transient response in the terminal current. Both these features appear to be in good agreement with the model proposed in refs. [11] and [12] where it is shown that the spin-polarization of the channel electrons is negligible in the parallel configuration but is much larger in the anti-parallel configuration and the resulting spin-flip current polarizes the Mn impurities. This is similar in principle to the well-known Overhauser effect (or dynamic nuclear polarization (DNP)) [82] but it is driven by the exchange interaction between the conduction band electrons in GaAs and localized Mn impurity spins rather than the hyperfine nuclear interaction. To our knowledge, neither (1) the dynamic impurity polarization nor (2) the use of anti-parallel spin-valves to drive it electrically (with no external magnetic field) have been demonstrated before.

Most significant advancements and Conclusions (include equations & figures as appropriate)

The heterostructure samples in the experiments are grown by molecular beam epitaxy on semi-insulating GaAs (001) substrate and consist of a ferromagnetic type-A manganese arsenide (MnAs) (60 nm) layer, n^+-doped ($\approx 10^{19}$ cm^{-3}) GaAs transition region (30 nm), and n-doped ($N_D \approx 10^{17}$ cm^{-3}) GaAs channel region (h = 500 nm), which is lightly co-doped with Mn impurities ($N_{Mn} \approx 1.4 \times 10^{16} cm^{-3}$). The growth procedure is as follows. A 500 nm GaAs:(Si,Mn) channel layer is grown at 580 °C on a (2×4)-reconstructed surface using a growth rate and V/III beam equivalent pressure ratio of 0.72 μm/hr and 25, respectively. A 30 nm graded-doping n^+-GaAs contact layer is then grown with the Mn flux shuttered to form a triangular tunnel barrier. The substrate temperature is ramped down to 400 .C under an As_4 over-pressure, and the surface reconstruction transitions to a c(4×4) pattern as indicated by reflection high-energy electron diffraction (RHEED). The As4 flux is shuttered, and the substrate temperature is ramped down to 200 °C. Once the temperature has stabilized, the surface is soaked with an As_4 flux of 5×10^{-6} Torr for 90 s to form a template suitable for growth of type-A MnAs [13]. A 60 nm MnAs film is grown using a low growth rate (10 nm/hr) and substrate temperature (200 °C) during deposition of the first few monolayers of MnAs. After the nucleation phase completes, the growth rate and substrate temperature are both increased to 40 nm/hr and 250 °C, respectively. Analysis of the RHEED pattern indicates growth of a type-A MnAs film with the following epitaxial relationship: [1120]MnAs//[110]GaAs.

The devices are fabricated by using conventional photolithography, dry etching, metal deposition and lift-off techniques. The Mn concentration in the channel is sufficiently low such that significant donor compensation or formation of MnAs precipitates cannot occur [13]. The effective donor density in the channel region is, $n_0 = N_D - N_{Mn} = 8.6 \times 10^{16}$ cm^{-3}. The Mn doping density is verified by secondary ion mass spectroscopy (SIMS), shown in Fig. 2. SQUID measurements on the (Si,Mn)-doped channel region does not show any hysteresis (shown in the inset to Fig. 2). This confirms the absence of ferromagnetism in the Mn-doped channel region. The lightly doped Mn atoms in GaAs behave as paramagnetic impurities [10,14]. Identical control devices without Mn impurities in the channel region were also fabricated and characterized. The heavily Si-doped (n^+) region beneath the MnAs contact pads forms a Schottky tunnel contact for efficient spin injection into semiconductors [15]. The basic MnAs/GaAs/MnAs spin-valve behavior of both Mn-doped spin-valves and control devices is confirmed through conventional and control measurements using a four probe ac lock-in

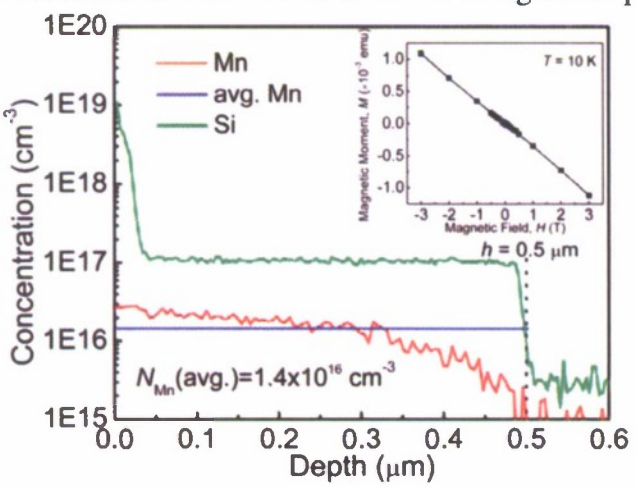

Figure 2: The doping densities of silicon (n-doping) and Mn versus channel depth are shown. Mn atoms behave as acceptors and partially compensate the n-doping. Inset shows the SQUID measurement on (Si,Mn) doped channel region grown on semi-insulating GaAs(001) substrate. The absence of remanent magnetization indicates lack of ferromagnetism in the channel region.

technique [8]. Figure 3 shows the measured magnetoresistance as a function of applied magnetic field H for a Mn-doped spin-valve. The two peaks correspond to the anti-parallel alignment of analyzer (A) and polarizer (P) at H = 500 G, which is confirmed by low temperature MOKE measurements, also shown in Fig. 3. A peak magnetoresistance of ~1.3%

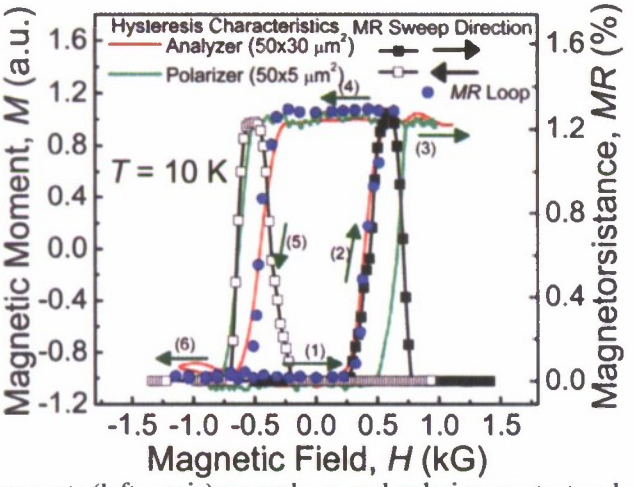

Figure 3: MOKE measurements (left y axis) on analyzer and polarizer contact pads, and magnetoresistance measurements on the Mn-doped spin-valves (right y axis) versus applied magnetic field at 10 K. The magnetoresistance data show two peaks which correspond to the antiparallel magnetization alignment of analyzer and polarizer contact pads. The MR loop closely follows the hysteresis of the analyzer contact pad. The arrows indicate the magnetic field sweep directions for the hysteresis plots. Contact pad magnetization data are shown for sweep (1)-(6). The MR loop is shown for sweep (1),(2),(4)-(6).

is measured at 10 K, which is close to the value reported earlier [8].

Transient current measurements are performed by mounting the samples in a cryostat, placed between the poles of an electromagnet. An in-plane variable magnetic field (along the magnetic easy axis of MnAs, GaAs [110] direction) is swept quasi-statically from -5 kG to 500 G, which sets the polarizer and analyzer magnetization in opposite directions (Fig. 8.3). The magnetic field is then swept back to zero. The polarizer and analyzer retain the anti-parallel magnetization configuration due to the remanence of ferromagnetic MnAs contact pads. A voltage bias is applied and the current through the device is measured as a function of time. Figure 5.4(a) shows the measured data for T = 10, 15 and 20 K. The current is initially large at 99.94 μA, before it saturates to a lower value of 98.86 μA at T = 10 K. The measurements are repeated for T = 15 and 20 K. It is observed that the relative change [$\Delta I = I(t = 0) - I(t = \infty)$] decreases from 1.08 μA to 0.55 μA as the temperature increases from 10 K to 15 K. The effect disappears for $T \geq 20$ K. No transient change in current was observed for control devices at all temperatures. The external magnetic field is zero during the transient measurements, which prevents spurious polarization of Mn impurities from external magnetic fields.

Similar measurements were carried out with polarizer and analyzer magnetized in the same direction. In this case, an in-plane -5 kG (larger than the coercivity of both the contact pads) magnetic field is applied to magnetize both contacts in the same direction. The magnetic field is then quasi-statically made zero. A pulse bias is applied as before and the transient

current through the device is measured. Figure 8.4(b) shows the measured current as a function of time at T = 10, 15 and 20 K. No noticeable change in the current level is observed under these conditions. Figure 8.4(c) shows the magnetoresistance, MR =(I_P - I_{AP})/I_{AP} as determined from Figs. 5.4(a) and (b).

Almost all the experimental features can be explained in terms of the circuit diagrams in Fig. 5 (adapted from Figs. 3(a) and (b) of ref. [12]), where the elements in the "shunt arm" g_{so}, g_γ and I_γ represent spin-flip processes that try to restore the imbalance in the electrochemical

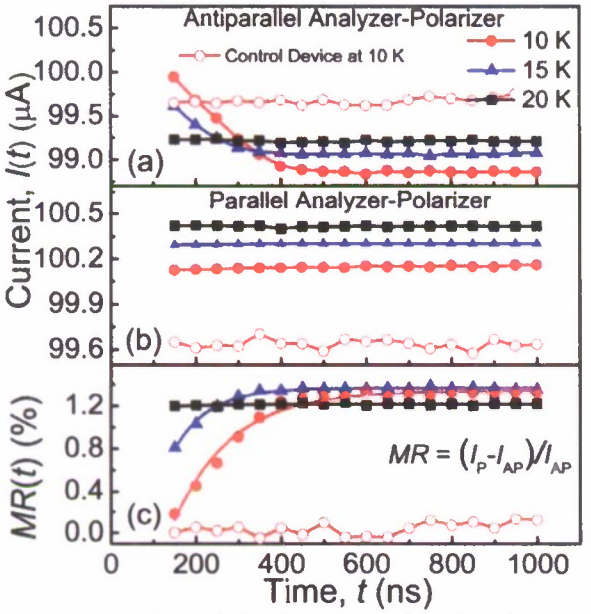

Figure 4: The measured transient current through the device as a function of time with (a) anti-parallel and (b) parallel magnetization of analyzer and polarizer contacts. The current is initially large before it saturates to a lower value for the anti-parallel configuration. No significant change is observed for the parallel configuration; (c) magnetoresistance, MR =(I_P -I_{AP})/I_{AP} as a function of time. The solid-lines show MR(t) as determined from the model using appropriate model parameters. An external trigger is generated at t = 0. There is a delay of ~150 ns for the voltage source and the electrometer to respond to this trigger, which leads to the the shift in the origin for the time axis by the same amount.

potentials $\mu_\uparrow$ and $\mu_\downarrow$ in the spin-up and spin-down channels. First, the transient terminal current is observed only for the anti-parallel configuration and not for the parallel configuration (Fig. 4). This can be understood by noting that the contact conductances, in the parallel configuration, form a balanced "Wheatstone Bridge" (Fig. 5(a)), which results in negligible potential difference $\mu_\uparrow$ - $\mu_\downarrow$ between spin-up and spin-down channel electrons. By contrast, the anti-parallel configuration results in a significant imbalance potential $\mu_\uparrow$ - $\mu_\downarrow$, which gives rise to spin-flip processes that polarize the impurities leading to transient behavior in the terminal current. Second, the terminal current in the anti-parallel configuration decays with time with a time-constant ~$(k_BT)^{-1}$: This is understood by noting that as the Mn impurities get polarized ($F_\uparrow$ - $F_\downarrow$ increases) the spin-flip current (through g_γ and I_γ) and hence the terminal current decreases.

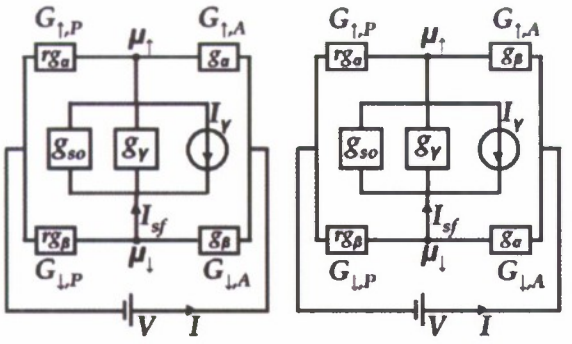

Figure 5: Equivalent circuit diagram of the SCT structure: g_γ , g_{so}, $G_{\uparrow(\downarrow),P}$, $G_{\uparrow(\downarrow),A}$, g_α, g_β, r, $\mu_{\uparrow(\downarrow)}$, and, I_{sf} are spin-flip conductance due to Mn impurity, spin-flip conductance independent of Mn impurity, polarizer conductance for up(down)-spin, analyzer conductance for spin-up(down) electrons, majority-spin tunnel conductance, minority-spin tunnel conductance, polarizer to analyzer area ratio, average chemical potential for spin-up(down) channel electrons, and, total spin-flip current respectively. The current source $I_\gamma \propto \int dE\{f_\uparrow (1 - f_\downarrow) + f_\downarrow (1 - f_\uparrow)\}(F_\uparrow - F_\downarrow)$, where, $f_{\uparrow(\downarrow)}$ and $F_{\uparrow(\downarrow)}$ are the average energy (E) distribution of spin-up (down) electrons having chemical potential $\mu_{\uparrow(\downarrow)}$ and fraction of impurities having up(down)-spin respectively.

So the transient behavior in the terminal current is, in essence, the signature of the dynamics of polarization ($F_\uparrow - F_\downarrow$) of the Mn impurity spins. Assuming that the Mn impurities have negligible spin-lattice-relaxation [10] the time constant (τ) for impurity polarization through exchange interaction with conduction band electrons has been shown, according to NEGF treatment, to be inversely proportional to $\int dE\{f_\uparrow (1 - f_\downarrow) + f_\downarrow (1 - f_\uparrow)\} \approx k_B T$ for $\mu_\uparrow - \mu_\downarrow < k_B T$ (Eqn. 5.6 and the associated discussion in [12]). Our model thus suggests that $\tau \sim (k_B T)^{-1}$ is in agreement with experiment (120 ns at 10 K, 80 ns at 15 K). As the temperature increases we expect the effect to get smaller because g_{so} increases (increased spin-orbit relaxation) while g_γ decreases (fewer Mn impurities are present within a spin-diffusion length which gets shorter with temperature). While this is in qualitative agreement with experimental observations we do not have a full quantitative explanation for the disappearance of the effect at 20 K. One of the possible reasons may be that the phonon assisted spin-lattice relaxation of Mn impurities in GaAs becomes dominant at the higher temperatures. Interestingly our model predicts that as $t \rightarrow \infty$ the Mn impurities get polarized and do not contribute to spin-flip scattering any more, suggesting that a spin-valve with and without Mn impurities should show approximately the same temperature dependent magnetoresistance determined by the spin-orbit term (g_{so}). This seems to be in agreement with experimental observations [8].

For a quantitative model, we have adopted two approaches: one based on the Non-equilibrium Green's Function (NEGF) method [12] and one based on the drift-diffusion method [16,17]. Both can be approximately mapped onto the circuit model of Fig. 5 and lead to similar quantitative results. Here we present results from the second model, which is based on the spin-diffusion equation,

$$D\frac{\partial^2 n_{\uparrow(\downarrow)}}{\partial x^2} = \frac{\partial n_{\uparrow(\downarrow)}}{\partial t} + \frac{n_{\uparrow(\downarrow)} - n_{\downarrow(\uparrow)}}{\tau_{\uparrow\downarrow(\downarrow\uparrow)}} + \frac{1}{e^2 h} G_{\uparrow(\downarrow)}\left[\mu_{\uparrow(\downarrow)} - eV\right] \qquad (1)$$

where D is the effective diffusion coefficient, $n_{\uparrow(\downarrow)}(x, t)$ is the spin-up (spin-down) electron density, $G_{\uparrow(\downarrow)}(x)$ is the spin-up (spin-down) tunnel conductance, V (x) is the applied voltage, and $\mu_{\uparrow(\downarrow)}(x, t)$ is the electrochemical potential for spin-up (spin-down) electrons. Also, the relation, $n_\uparrow (x, t) + n_\downarrow (x, t) = n_0$ holds. The time dependence of the spin-.ip current, $I_{sf} = I_{\uparrow,A} - I_{\uparrow,P}$ with spin-dynamics is determined by integrating Eqn. 1 as:

$$\frac{1}{e}[I_{\uparrow,A}(t) - I_{\downarrow,P}(t)] = \frac{\partial N_{\uparrow}}{\partial t} + \frac{N_{\uparrow} - N_{\downarrow}}{\tau_{\uparrow(\downarrow)}} \quad (2)$$

where $N_{\uparrow(\downarrow)}$ are the total number of spin-up (spin-down) electrons in the channel. Equation 2 helps to decouple the spin-scattering due to Mn impurities and the scattering due to Mn-independent processes. We define a parameter ß which correlates $n_{\uparrow(\downarrow)}$ with $\mu_{\uparrow(\downarrow)}$ through Fermi-Dirac distribution and density-of-states functions, and which is approximated by a linear function obtained from Taylor series expansion as,

$$\beta = \frac{n_{\uparrow(\downarrow)} - n_0/2}{\mu_{\uparrow(\downarrow)} - \mu_0} = \left[\frac{\partial n_{\uparrow(\downarrow)}}{\partial \mu_{\uparrow(\downarrow)}}\right]_{\mu_{\uparrow(\downarrow)}=\mu_0} \quad (3)$$

where μ_0 is the electrochemical potential for the unpolarized electrons, $n_{\uparrow} = n_{\downarrow} = n_0/2$. The high doping in the channel, large contact resistance and low bias operation lead to negligible drift in these devices [17]. The model parameters, determined at 10 K, are as follows: (1) from Hall measurements, μ = 3000 cm2/V.s; (2) from the Fermi integral, $De/\mu k_B T = 8.3$ [17]; (3) tunnel conductance and spin-selectivity of the tunnel barrier are determined by analyzing the experimentally measured magnetoresistance data (assuming $\tau_{\uparrow\downarrow} = \tau_{\downarrow\uparrow} = 13$ ns [18]) with the spin-diffusion model. Thus $G_{\uparrow} + G_{\downarrow} = 2.5 \times 10^7\ \Omega^{-1}m^{-2}$ [19]; (4) from Fermi-Dirac distribution and density-of-states functions, $\beta = 0.2 \cdot (n_0/2k_B T)$.

Figure 6(a) shows the estimated time dependence of the spin-flip current in the antiparallel configuration as determined by using Eqns.1 and 2 on the experimental data shown in Fig. 4. Note that the change in spin-flip current ΔI_{sf} at different temperatures is larger than the change in the terminal current .I, as we would expect from the circuit diagram of Fig. 5 which

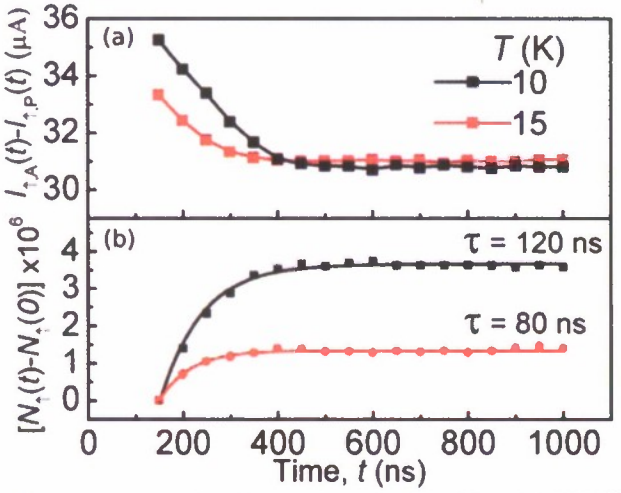

Figure 6: (a) Estimated spin-flip current as a function of time, for T = 10 and 15 K. The spin capacitive effect is reduced at higher temperatures due to enhanced spin-relaxation from native GaAs lattice atoms; (b) charging of Mn paramagnetic spin as a function of time.

gives $\Delta I_{sf}/\Delta I = (1/P_c)\{1 + (r - 1)^2(1 - P_C^2)/(4r)\}$, where, $P_c = (g_{\alpha} - g_{ß})/(g_{\alpha} + g_{ß}) = (G_{\uparrow} - G_{\downarrow})/(G_{\uparrow} + G_{\downarrow})$. Using experimental values (P_c =0.39 and r =1/6) we find $\Delta I_{sf}/\Delta I$ to be 4.8, which is reasonably close to the value of 3.6 obtained from the detailed numerical calculation (see Figs. 4 and 6). Time constants (τ) associated with the charging of the spin-capacitor (Fig. 6(b)) as determined by using Fig. 6(a) and Eqn. 2 are found to be 120 ns and 80 ns at 10 K and 15 K, respectively. The estimated value for τ (120 ns) is close to the value of the spin-spin relaxation

time-constant (100 ns) reported earlier for an interaction between conduction electron spin and a paramagnetic defect in a silicon field-effect-transistor [19].

References

[1] I. Z˘ utic´, J. Fabian, and S. D. Sarma, Rev. Mod. Phys. 76, 323 (2004).
[2] F. J. Jedema, A. T. Filip, and B. J. van Wees, Nature (London) 410, 345 (2001).
[3] M. Johnson and R. H. Silsbee, Phys. Rev. Lett. 55, 1790 (1985).
[4] D. Saha, M. Holub, and P. Bhattacharya, Appl. Phys. Lett. 91, 072513 (2007).
[5] X. Lou, C. Adelmann, S. A. Crooker, E. S. Garlid, J. Zhang, K. S. M. Reddy, S.D. Flexner, C. J. Palmstrom, and P. A. Crowell, Nature Phys. 3, 197 (2007).
[6] J. A. Katine, F. J. Albert, R. A. Buhrman, E. B. Myers, and D. C. Ralph, Phys. Rev. Lett. 84, 3149 (2000).
[7] M. Holub, J. Shin, D. Saha, and P. Bhattacharya, Phys. Rev. Lett. 98, 146603 (2007).
[8] D. Saha, M. Holub, P. Bhattacharya, and Y. C. Liao, Appl. Phys. Lett. 89, 142504 (2006).
[9] V. Garcia, H. Jaffre`s, J.-M. George, M. Marangolo, M. Eddrief, and V. H. Etgens, Phys. Rev. Lett. 97, 246802 (2006).
[10] N. Almeleh and B. Goldstein, Phys. Rev. 128, 1568 (1962).
[11] S. Datta, Appl. Phys. Lett. 87, 013115 (2005).
[12] S. Datta, From Nanostructures to Nanosensing Applications, Proceedings of the International School of Physics ''Enrico Fermi,'' Course CLX, edited by A. D'Amico, G.
Balestrino, and A. Paoletti (IOS, Amsterdam, 2005), p. 1.
[13] R. Moriya and H. Munekata, J. Appl. Phys. 93, 4603 (2003).
[14] M. Kaminskai, A. Twardowski, and D. Wasik, J. Mater. Sci., doi:10.1007/s10854-007-9486-z (2007).
[15] E. I. Rashba, Phys. Rev. B 62, R16267 (2000).
[16] H. Dery, L. Cywinski, and L. J. Sham, Phys. Rev. B 73, 041306(R) (2006).
[17] Z. G. Yu and M. E. Flatte´, Phys. Rev. B 66, 235302 (2002).
[18] R. I. Dzhioev, K.V. Kavokin, V. L. Korenev, M.V. Lazarev, B.Y. Meltser, M.N. Stepanova, B. P. Zakharchenya, D. Gammon, and D. S. Katzer, Phys. Rev.
B 66, 245204 (2002).
[19] M. Xiao, I. Martin, E. Yablonovitch, and H.W. Jiang, Nature (London) 430, 435 (2004).

4. A Monolithically Integrated Magneto-Opto-Electronic Circuit

Comprehensive Summary of the significant work accomplished

Semiconductor spintronics is aimed at improving the operation and functionality of conventional devices in terms of speed, power and packing density [1-3]. Significant advances in this area have been made, such as the demonstration of discrete devices like spin-valves [4-7], spin-current amplifiers [8], spin capacitors [9], spin LEDs [10], and spin lasers [11] using ferromagnet/semiconductor heterostructures. Most of these devices have been demonstrated with GaAs-based platforms, on which matured microelectronic and optoelectronic technologies also exist. For future applications with new paradigms and functionalities, it is of interest and importance to monolithically integrate spintronic devices with microelectronic and optoelectronic devices, to form a MOEIC. To cite a couple of applications, the spintronic devices will make the MOEICs inherently reprogrammable and will enable them to be included in the important class of reconfigurable integrated circuit (IC). The MOEIC will also allow spin information to be transmitted over distances much longer than the spin-diffusion length. In analogy with micro-electro-mechanical systems (MEMS), the integration of spintronic devices with other conventional devices can have multiple benefits. We demonstrate here, for the first time, the characteristics of a MOEIC on GaAs, which is realized by the monolithic integration of a spin valve, an amplifier circuit containing high electron mobility transistors (HEMTs) and passive elements, and a LED. Variation of magnetic information is amplified and read out by photons emitted by the LED.

The integration of magnetic, optoelectronic and electronic devices is facilitated by the fact that the fabrication steps for semiconductor spintronic devices are analogous to the conventional micro-fabrication techniques. We present here an MOEIC wherein a lateral semiconductor spin-valve, a cascaded HEMT amplifier and an LED are monolithically integrated to demonstrate a magneto-electronic switch. A spin-valve has two ferromagnetic contacts acting as polarizer and analyzer [4]. The resistance of the spin-valve is low if both polarizer and analyzer are magnetized in the same direction and high if they are magnetized in opposite directions. The magnetoresistance resulting from parallel to anti-parallel magnetization configurations is usually small and at times difficult to detect. The cascaded HEMT amplifier in the integrated circuit amplifies the magnetoresistance [15]. A change in the gate-to-source voltage of the HEMT changes the drain-to-source current and hence the device acts as a transconductance amplifier. A cascaded configuration is used to increase the amplifier gain. The large change in the current of the second HEMT is used to drive the LED. The light intensity of the LED changes in proportion to the change in the drain-to-source current [16] of the second HEMT. Hence, the circuit operation can be described in the following sequential steps: (1) a magnetic field (H) changes the resistance of the spin-valve; (2) the magnetoresistance is amplified by the cascaded HEMT ampli.er to a large change in current; and (3) the LED light intensity is modulated by the changing current. The MOEIC therefore converts the spin-polarization in the channel region of the lateral spin-valve to an equivalent change in light intensity of the LED. The circuit operates as a magneto-electronic switch which modulates the light intensity of the LED.

Most significant advancements and Conclusions (include equations & figures as appropriate)

The circuit diagram of the MOEIC is shown in Fig. 1. The spin-valve [resistance R(H)] and resistor R_1 are connected in series between gate and source terminals of the first HEMT ($HEMT_1$). A current bias I_B is applied, which creates a gate-to-source bias voltage, $V_{GS1} = I_B(R + R_1)$. A small change in resistance ΔR (magnetoresistance, MR = $\Delta R/R$) changes V_{GS1} by v_{gs1},

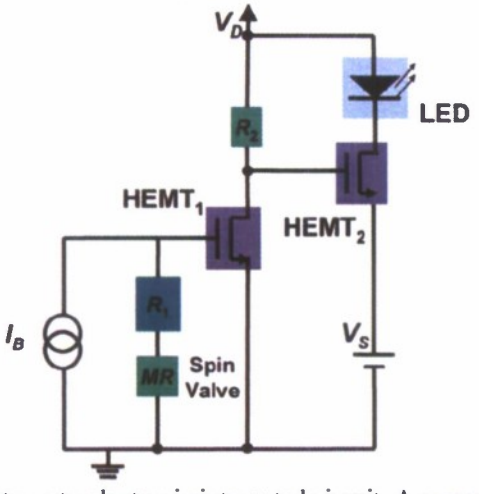

Figure 1: A schematic of the magneto-opto-electronic integrated circuit. A magnetic field changes the resistance of the spin-valve. The magnetoresistance is amplified by the cascaded transconductance HEMT amplifier to a large change in drain-to-source current which modulates the light intensity of the LED. The resistors R1 and R2 are used to correctly bias the cascaded HEMT amplifier in the linear region.

which in turn changes the drain-to-source current, I_{DS1} by i_{ds1}. These quantities are related by the transconductance ($g_{m1} = \partial I_{DS1}/\partial V_{GS}$) of $HEMT_1$ as, $i_{ds1} = g_{m1}v_{gs1} = I_B(g_{m1}\Delta R)$, where $g_{m1}\Delta R$ is the gain of the first stage of the cascaded amplifier. The output of $HEMT_1$ is connected to the gate terminal of $HEMT_2$. The change in the gate-to-source voltage of $HEMT_2$ is given by, $v_{gs2} = -i_{ds1}R_2$, where R_2 is the bias resistor in the $HEMT_1$ drain terminal. The negative sign is due to the fact that an increase in i_{ds1} decreases v_{gs2}. The gain of the second stage amplifier is $g_{m2}R_2$, where g_{m2} is the transconductance of $HEMT_2$. The change in the drain-to-source current of $HEMT_2$ is therefore given by $i_{ds2} = -I_B(g_{m1}\Delta R)(g_{m2}\Delta R)$, which is also the change in the current flowing through the LED. If the slope of the light-output versus input-current (L–I) characteristics of the LED is η ($=\Delta L/\Delta I$), the resultant change in the light output is given by,

$$\Delta L = -I_B [g_{m1}\Delta R][g_{m2}R_2]\eta \quad (1)$$

Hence, the change in the light intensity is directly proportional to the change in resistance in the linear region of operation of the amplifier. If the quiescent (Q) drain-to-source current of HEMT2 is $I_{DS2,Q}$, the fractional change in light intensity is given by,

$$\Delta L/L_0 = -I_B [g_{m1}\Delta R][g_{m2}R_2]\, \eta\, /L(I_{DS2,Q}) \quad (2)$$

where $L_0 = L(I_{DS2,Q})$ is the light-output at the quiescent drain-to-source current $I_{DS2,Q}$. When the amplifier operates in the linear region, $HEMT_2$ operates in the saturation region. $I_{DS2,Q}$ is therefore independent of R and the fractional change in light intensity (Eqn. 2) is also independent of R. Hence, the magnetoresistance amplification is primarily dependent on the external circuit parameters and independent of the absolute value of MR.

A schematic of the MOEIC heterostructure grown by molecular beam epitaxy (MBE) is shown in Fig. 2. The heterostructure consists of epitaxially grown layers for the MnAs/GaAs

lateral spin-valve [4], the GaAs/$Al_{0.2}Ga_{0.8}As$ multi-quantum-well LED [16], and the $Al_{0.2}Ga_{0.8}As$/ $In_{0.2}Ga_{0.8}As$ pseudomorphic HEMT [15], all separated by undoped GaAs buffer

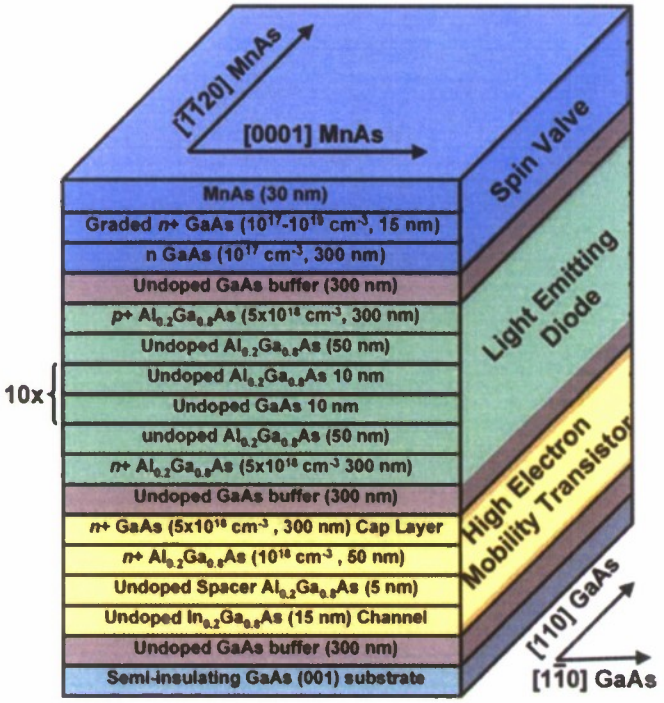

Figure 2: A schematic of the MOEIC heterostructure grown by MBE. The heterostructure consists of epitaxially grown layers for the MnAs/GaAs lateral spin-valve, the GaAs/$Al_{0.2}Ga_{0.8}As$ multi-quantum-well LED and the $Al_{0.2}Ga_{0.8}As$/$In_{0.2}Ga_{0.8}As$ pseudomorphic HEMT separated by undoped GaAs buffer layers.

layers. The spin-valve is grown as the last (uppermost) device which has ferromagnetic MnAs as the top layer. This avoids the necessity for epitaxial growth on MnAs, which is very difficult. The LED heterostructure is grown beneath the spin-valve to minimize out-diffusion of Be from the p-doped layer during subsequent thermal cycling. The heterostructure for the HEMT is grown first and is therefore at the bottom. The fabrication of the MOEIC circuit is done in the following sequence: spin-valve, resistance R_1, LED, HEMT, resistance R_2, interconnect and contact metallization. The nominal value for R_1 and R_2 are designed to be 175 Ω and 1 kΩ, respectively. Figures 3(a) and (b) show a three-dimensional (3D) schematic and a micro-photograph (before the final interconnect and metallization steps) of the MOEIC, respectively. The circuit layout ensures good surface morphology. Circuits with additional contact terminals for individual access to the circuit elements are also fabricated to trace signal flow as it moves from input to output. Control devices were also fabricated to confirm spin dependency of the observed effects.

Measurements are done by mounting the MOEIC samples in a cryostat, placed between the poles of an electromagnet. Figure 4 (a) shows the spin-valve characteristics as the magnetic field is varied from -2 kG to 2 kG. It can be seen that the resistance is low when polarizer and analyzer are magnetized in the same direction for large magnetic fields and high when they are magnetized in opposite directions ($|H|$ = 1.2 kG). A peak magnetoresistance of 0.33% is measured at 20 K. The Hanle effect (spin precession in a perpendicular magnetic field) measurement were also done to ensure spin

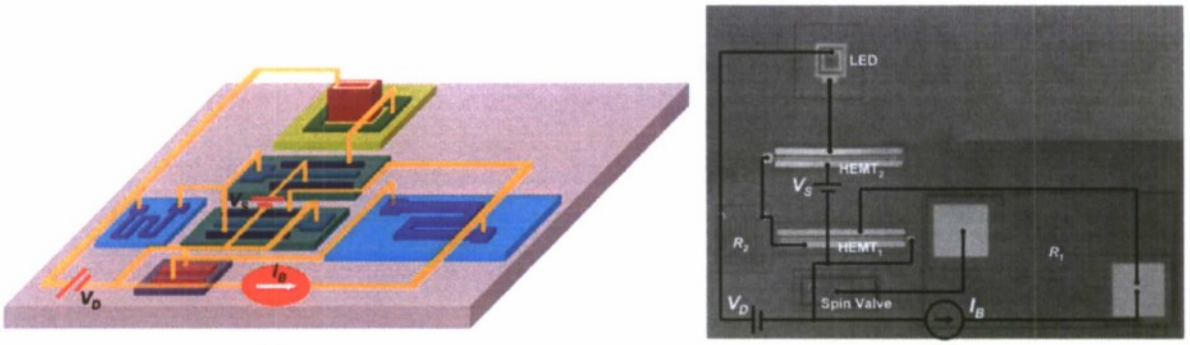

(a) (b)

Figure 3: (a) A schematic and (b) a micro-photograph of the fabricated MOEIC (before the final interconnection and metallization step). The resistors R1 and R2 are delineated on undoped GaAs buffer layers by physical vapor deposition and lift-off technique.

dependency of the observed effect (Fig. 4(b)). The measured magnetoresistance is smaller than reported earlier [19] and is due to the fact that annealing of HEMT source and drain contacts introduces undesirable MnAs/GaAs interface mixing, which reduces spin injection and detection efficiencies. Control measurements were also done to ensure spin dependency of the effect [4,8]. Figures 5(a) and (b) show the measured characteristics of an isolated HEMT which has undergone all the processing steps as the MOEIC. Figure 5(a) shows g_m as a function V_{GS} for V_{DS} = 2 V . measurements were also done to ensure spin dependency of the effect [19, 71, 114]. Figures 8.5(a) and (b) show the measured characteristics of an isolated HEMT which has undergone all the processing steps as the MOEIC. Figure 8.5(a) shows g_m as a function V_{GS} for V_{DS} = 2 V .

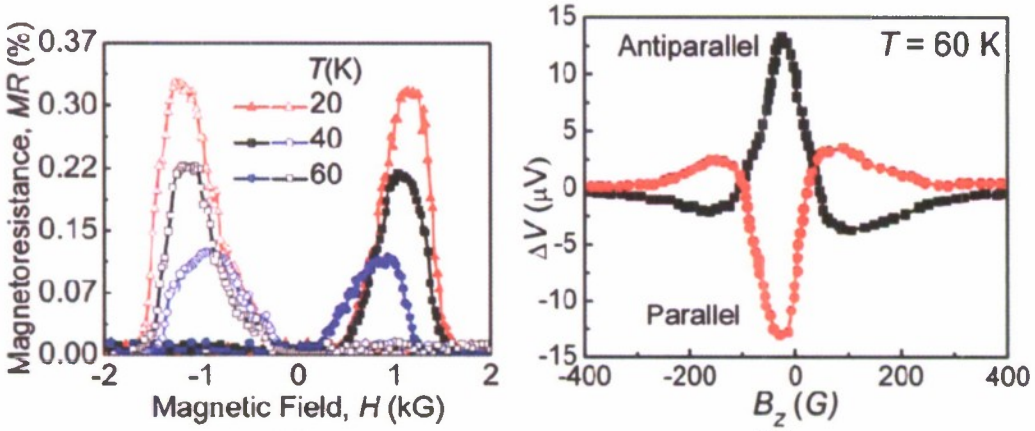

(a) (b)

Figure 4: (a) The spin-valve shows two magnetoresistance peaks corresponding to the case whenthe polarizer and the analyzer are magnetized in opposite directions. The magnetoresistance decreases with increasing temperature due to decreasing spin-relaxation time; (b) non-local voltage as a function of perpendicular magnetic field in a spin-valve. The spin precesses due to Hanle effect which leads to the change in spin accumulation. The asymmetry is due to a small misalignment of the sample and presence of a small axial magnetic field.

The threshold voltage V_{TH} is determined to be -1.9 V. Figure 5(b) depicts gm as a function of temperature for V_{DS} = 2 V. These characteristics confirm that the HEMTs function as a voltage controlled current source. Figure 6(a) shows the measured L–I and I–V characteristics of an LED. Figure 6(b) shows the L–I characteristics as a function of temperature. The quantum efficiency and hence η increases with decreasing temperature. The individual circuit elements,

therefore, exhibit the desired characteristics. It is also observed that the HEMT and LED characteristics do not change for magnetic fields $|H| \leq 3$ kG.

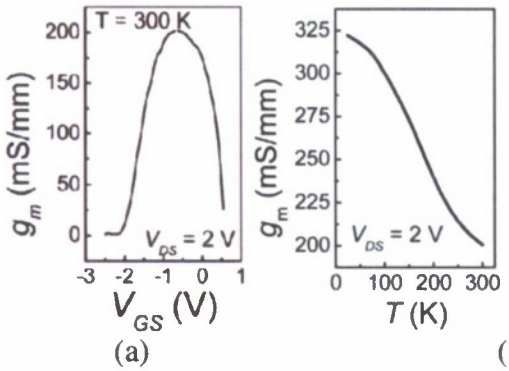

Figure 5: (a) Transconductance gm of the HEMT as a function of gate-to-source voltage. It reaches peak at V_{GS} = -0.9 V; (c) transconductance of the HEMT as a function temperature. It increases with decreasing temperature due to increasing mobility.

The MOEIC circuit operation is then measured by biasing it with voltage and current sources, as shown in Fig. 1. Both the HEMTs are biased with, $V_{GS1,Q} = V_{GS2,Q}$ = -1.5 V and $V_{DS1,Q} = V_{DS2,Q}$ = 2 V at 40 K. Transconductances g_{m1} and g_{m2} are then both equal to 175 mS/mm under this bias condition. Consequently, the quiescent currents through the HEMTs and LED are equal and are given by $I_{DS1,Q} = I_{DS2,Q} = I_{LED} \approx 5$ mA. The measured $R \approx 2.17$ kΩ, and hence a current bias $I_B = V_{GS1,Q}/(R + R_1)$ = -640 μA is applied to the input terminal. The drain bias voltage V_D is determined as, $V_D = I_{DS1,Q} R2 + V_{DS1,Q}$ = 7 V. The source voltage for $HEMT_2$ is then determined as, $V_S = V_{DS1,Q} - V_{GS2,Q}$ = 3.5 V. The voltage across the LED is given by, $V_{LED} = V_D - V_{DS2,Q} - V_S$ = 1.5 V. It is to be noted from the I–V characteristics in Fig. 6(a) that $I_{LED}(V_{LED} = 1.5\ V) \approx 5$ mA = $I_{DS2,Q}$. Hence, the circuit is correctly biased at a stable operating point. A magnetic field is then swept and the LED light intensity is measured as a function

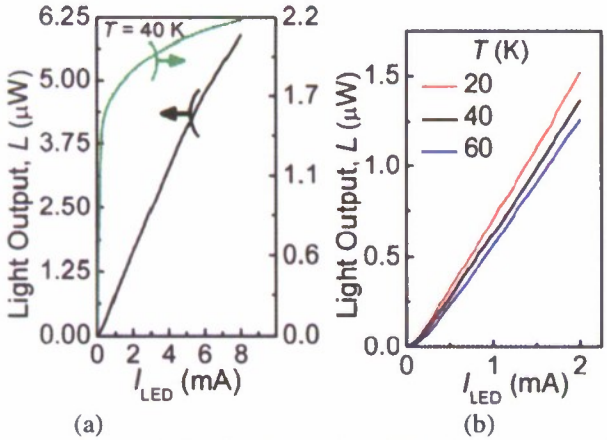

Figure 6: (a) LED light output and terminal voltage as a function of bias current; (b) light output versus bias current of the LED as a function of temperature. The quantum efficiency increases with decreasing temperature, hence, the slope increases.

of H at various temperatures with a silicon photodetector (Fig. 7). The light intensity

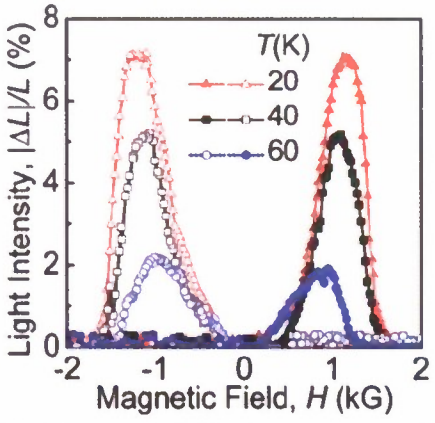

Figure 7: MOEIC characteristics. Modulation of LED light intensity as a function of magnetic field. The light intensity modulation shows exactly the same magnetic field dependence as the spin-valve characteristics. The magnetoresistance amplification is determined to be ≈ 20 in the region of operation. The MOEIC acts as a magneto-electronic switch which varies LED light intensity in response to an external magnetic field.

modulation shows exactly the same magnetic field dependence as the spin-valve characteristics, as predicted by Eqn. 2. This confirms the spin-dependency of the observed change. The overall MOEIC gain, $(R/L)\times(\partial L/\partial R)$ is determined to be ~20 in the temperature range of operation. As expected, the MOEIC amplifies the magnetoresistance of the spin-valve and acts as a magneto-electronic switch which modulates the LED light intensity in response to a varying magnetic field. The modulated light intensity, which can be transmitted over a long distance, bears the signature of spin-polarization in the spin-valve channel region.

References:

[1]. S. A. Wolf, D. D. Awschalom, R. A. Buhrman, J. M. Daughton, S. von Molnar, M. L. Roukes, A. Y. Chtchelkanova, and D. M. Treger, *Science* **294**, 1488 (2001).

[2]. I. Žutić, J. Fabian, and S. Das Sarma, *Rev. Mod. Phys.* **76**, 323 (2004).

[3]. See: http://www.itrs.net/reports.html, 2004.

[4]. D. Saha, M. Holub, P. Bhattacharya, and Y. C. Liao, *Appl. Phys. Lett.* **89**, 142504 (2006).

[5]. X. Lou, C. Adelmann, S. A. Crooker, E. S. Garlid, J. Zhang, K. S. M. Reddy, S. D. Flexner, C. J. Palmstrom, and P. A. Crowell, *Nat. Phys.* **3**, 197 (2007).

[6]. I. Appelbaum, B. Huang, and D. J. Monsma, *Nature (London)* **447**, 295 (2007).

[7]. O. M. J. van 't Erve, A. T. Hanbicki, M. Holub, C. H. Li, C. Awo-Affouda, P. E. Thompson, and B. T. Jonker, *Appl. Phys. Lett.* **91**, 212109 (2007).

[8]. D. Saha, M. Holub, and P. Bhattacharya, *Appl. Phys. Lett.* **91**, 072513 (2007).

[9]. D. Saha, L. Siddiqui, P. Bhattacharya, S. Datta, D. Basu, and M. Holub, *Phys. Rev. Lett.* **100,** 196603 (2008).

[10]. C. H. Li, G. Kioseoglou, O. M. J. van 't Erve, M. E. Ware, D. Gammon, R. M. Stroud, B. T. Jonker, R. Mallory, M. Yasar, and A. Petrou, *Appl. Phys. Lett.* **86**, 132503 (2005).

[11]. M. Holub, J. Shin, D. Saha, and P. Bhattacharya, *Phys. Rev. Lett.* **98**, 146603 (2007).

[12]. Y. He, Q. Zhang, A. V. Nurmikko, J. Slaughter, R. W. Dave, and S. Tehrain, *Electron. Lett.* **37**, 1459 (2001).

[13]. I. Appelbaum, K. J. Russell, D. J. Monsma, V. Narayanamurti, C. M. Marcus, M. P. Hanson, and A. C. Gossard, *Appl. Phys. Lett.* **83,** 4571 (2003).

[14]. N. Itoh, H. Minemoto, D. Ishiko, and S. Ishizuka, *Appl. Opt.* **38**, 2047 (1999).

[15]. F. Ali and A. Gupta, *HEMTs and HBTs: Devices, Fabrication, and Circuits (Artech House, Boston,* 1991).

[16]. P. Bhattacharya, Semiconductor Optoelectronic Devices (*Prentice-Hall, Englewood Cliffs,* NJ, 1996).

[17]. J. Li, B. Huang, and I. Appelbaum, *Appl. Phys. Lett.* **92**, 142507 (2008).